Atmos. Chem. Phys. Discuss., 13, 6067–6129, 2013
www.atmos-chem-phys-discuss.net/13/6067/2013/
doi:10.5194/acpd-13-6067-2013

Atmospheric Chemistry and Physics Discussions

Sensitivity of tropospheric chemical composition to halogen-radical chemistry using a fully coupled size-resolved multiphase chemistry/global climate system – Part 1: Halogen distributions, aerosol composition, and sensitivity of climate-relevant gases

M. S. Long[1], W.C. Keene[2], R. C. Easter[3], R. Sander[4], X. Liu[3], A. Kerkweg[5], and D. Erickson[6]

[1]School of Engineering and Applied Sciences, Harvard University, Cambridge, MA, USA
[2]Department of Environmental Sciences, University of Virginia, Charlottesville, VA 22904, USA
[3]Atmospheric Sciences and Global Change Division, Pacific Northwest National Laboratory, Richland, Washington, USA
[4]Air Chemistry Department, Max-Planck Institute of Chemistry, 55020 Mainz, Germany
[5]Institute for Atmospheric Physics, University of Mainz, 55099 Mainz, Germany

[6]Computer Science and Mathematics Division, Oak Ridge National Laboratory, Oak Ridge, TN, USA

Received: 24 January 2013 – Accepted: 18 February 2013 – Published: 7 March 2013

Correspondence to: M. S. Long (mlong@seas.harvard.edu)

Published by Copernicus Publications on behalf of the European Geosciences Union.

ACPD
13, 6067–6129, 2013

Abstract

Observations and model studies suggest a significant but highly non-linear role for halogens, primarily Cl and Br, in multiphase atmospheric processes relevant to tropospheric chemistry and composition, aerosol evolution, radiative transfer, weather, and climate. The sensitivity of global atmospheric chemistry to the production of marine aerosol and the associated activation and cycling of inorganic Cl and Br was tested using a size-resolved multiphase coupled chemistry/global climate model (National Center for Atmospheric Research's Community Atmosphere Model (CAM); v3.6.33). Simulation results showed strong meridional and vertical gradients in Cl and Br species. The simulation reproduced most available observations with reasonable confidence permitting the formulation of potential mechanisms for several previously unexplained halogen phenomena including the enrichment of Br^- in submicron aerosol, and the presence of a BrO maximum in the polar free troposphere. However, simulated total volatile Br mixing ratios were generally high in the troposphere. Br in the stratosphere was lower than observed due to the lack of long-lived organobromine species in the simulation. Comparing simulations using chemical mechanisms with and without reactive Cl and Br species demonstrated a significant temporal and spatial sensitivity of primary atmospheric oxidants (O_3, HO_x, NO_x), CH_4, and non-methane hydrocarbons (NMHC's) to halogen cycling. Simulated O_3 and NO_x were globally lower (65 % and 35 %, respectively, less in the planetary boundary layer based on median values) in simulations that included halogens. Globally, little impact was seen in SO_2 and non-sea-salt SO_4^{2-} processing due to halogens. Significant regional differences were evident: the lifetime of nss-SO_4^{2-} was extended downwind of large sources of SO_2. The burden and lifetime of DMS (and its oxidation products) were lower by a factor of 5 in simulations that included halogens, versus those without, leading to a 20 % reduction in nss-SO_4^{2-} in the Southern Hemisphere planetary boundary layer based on median values.

ACPD
13, 6067–6129, 2013

1 Introduction

The development of comprehensive global Earth system models that are able to accurately simulate the climate system requires detailed understanding and treatment of multiphase atmospheric processes relevant to aerosol evolution and radiative transfer. However, due in part to limitations in computational power relative to numerical needs, most current Earth system models treat the physicochemical processing of size-resolved aerosols using parameterizations that are computationally conservative but, in many respects, inadequate to reliably characterize aerosol-climate interactions. These limitations contribute to the large uncertainties in the radiative effects of atmospheric aerosols, which are among the major factors that constrain our current understanding of and ability to predict global climate change.

Reliable simulation of the physical and chemical evolution of aerosols in the Community Earth System Model (CESM) and other Earth systems models requires explicit evaluation of processes as a function of size. Because of direct physical feedbacks, representative simulation of climatic influences also requires an interactive online scheme for aerosol microphysics and multiphase chemistry. A number of major issues must be considered to implement such a scheme. Direct interactions between relatively long-lived and fast-reacting species coupled with large concentration and size gradients of both aerosols and important related atmospheric constituents such as water vapor (e.g. Kerkweg et al., 2007), introduces a high degree of numerical stiffness that is unevenly distributed across the gridded model domain.

The size- and composition-dependent properties of aerosols significantly influence radiative fluxes through the atmosphere via two sets of interrelated processes. First, aerosols scatter and absorb incident and outgoing radiation and thereby directly influence net radiative transfer through the atmosphere and the associated distribution and partitioning of heat (and related kinetic and thermodynamic properties). Second, aerosols act as cloud condensation nuclei (CCN) and thereby influence the microphysical properties of clouds including droplet number, size distribution, and lifetime.

ACPD
13, 6067–6129, 2013

Through this latter set of processes, aerosols indirectly regulate radiative transfer via the associated modulation of physicochemical evolution and albedo of clouds. These processes also influence precipitation fields and, thus, the hydrologic cycle and related climatic feedbacks.

Aerosols also interact directly in the cycling and associated climatic effects of important tropospheric gases, particularly over the ocean. The production from marine-derived precursors and multiphase cycling of halogen radicals represents a significant net sink for ozone in the remote marine boundary layer (MBL) (Dickerson et al., 1999; Galbally et al., 2000; Nagao et al., 2000; Sander et al., 2003; Pszenny et al., 2004; Keene et al., 2009) and a potentially important net source in polluted coastal (Tanaka et al., 2003; Osthoff et al., 2008) and continental air (Thornton et al., 2010). The associated formation and scavenging of halogen nitrates accelerates the conversion of NO_x to HNO_3 and particulate NO_3^- thereby contributing to net O_3 destruction (Sander et al., 1999; Pszenny et al., 2003; Keene et al., 2009). Marine-derived halogen radicals (BrO and atomic Cl) oxidize $(CH_3)_2S$ (dimethyl sulfide, DMS) in the gas phase (Toumi, 1994; Keene et al., 1996; Saiz-Lopez et al., 2004) and hypohalous acids oxidize S(IV) in aerosol solutions (Vogt et al., 1996; Keene et al., 1998; von Glasow et al., 2002; von Glasow and Crutzen, 2004). The large surface area of primary marine aerosols also competes efficiently with nuclear clusters (from gas-to-particle reactions) for condensable reaction products from the oxidation of gaseous precursors (including H_2SO_4 from SO_2 oxidation) thereby diminishing the potential for clusters to grow to sustainable size. Consequently, the climatic influences of sulfur cycling may be substantially less than predicted based on models that do not explicitly evaluate interactions involving primary marine aerosols. Chlorine radicals also oxidize methane (an important greenhouse gas) (Platt et al., 2004; Lawler et al., 2009) and non-methane hydrocarbons (Keene et al., 2007; Pszenny et al., 2007), which leads to the production of condensable organic compounds that contribute to aerosol growth and, in the presence of sufficient NO_x, peroxy radicals that enhance oxidation potential. The photochemical processing of marine-derived organic compounds is an important source of OH and other radicals

ACPD
13, 6067–6129, 2013

that enhance oxidation potential within aerosol solutions (McDow et al., 1996; Zhou et al., 2006; Anastasio et al., 2007).

In terms of mass flux, bursting bubbles produced by breaking waves at the ocean surface are the largest source of aerosols in Earth's atmosphere (Andreae and Rosenfeld, 2008). The nascent droplets dehydrate into equilibrium with ambient water vapor and undergo other rapid (seconds) multiphase transformations involving the scavenging of gases, aqueous and surface reactions, and volatilization of products. (e.g. Chameides and Stelson, 1992; Erickson et al., 1999; Sander et al., 2003). The sub-μm fractions dominate number concentrations and associated direct and indirect influences on radiative transfer and climate (e.g. O'Dowd et al., 1997).

In this paper, the sensitivity of global atmospheric chemistry to the production of marine aerosol and the associated activation and cycling of inorganic Cl and Br was tested using a 3-mode size-resolving aerosol module (Modal Aerosol Module) version of the three-dimensional (3-D) National Center for Atmospheric Research's Community Atmosphere Model (CAM version 3.6.33; Gent et al., 2009; Liu et al., 2012; hereafter referred to as modal-CAM) coupled to the multiphase chemical module MECCA (Module Efficiently Calculating the Chemistry of the Atmosphere; Sander et al., 2005). The companion paper by Long et al. (2013) describes the coupled modeling system in detail. A follow-up manuscript will evaluate the sensitivity of climate to halogen cycling and the implications of multiphase processes for aerosol populations and cloud microphysical properties.

2 Model description

Atmospheric processes were simulated in 3-D using modal-CAM at $1.9^{\circ} \times 2.5^{\circ}$ lat-long resolution with 26 vertical levels (Gent et al., 2009). Modal-CAM is a FORTRAN90 compliant general circulation system built upon an extensive set of high-performance computational routines to preserve scalability and performance of the model across changes in resolution and model physics.

ACPD
13, 6067–6129, 2013

The dynamical core (approximation of the equations of motion on a discrete, spherical grid) is based on a flux-form semi-Lagrangian method better suited for tracer transport. This approach permits grid-wide stability of the chemistry solution, in contrast to discrete methods that introduce large dispersion and diffusion errors in their approximation of the equations of motion which propagate into and destabilize the chemistry solver.

Modal-CAM incorporates a comprehensive set of processes that control the evolution and coupling of three fixed-width log-normally distributed aerosol modes (Aitken, accumulation and coarse). The modal aerosol treatment is described in detail in Liu et al. (2012). Each mode consists of internally mixed populations of non-sea-salt (nss) SO_4^{2-}, organic matter from primary sources (OM), secondary organic aerosol (SOA) from volatile organic precursors, black carbon (BC), inorganic sea salt, and mineral dust. The nss-SO_4^{2-} is assumed to be in the form of NH_4HSO_4. OM and BC are treated only in the accumulation mode. SOA is only in the Aitken and accumulation modes, and mineral dust is only in the accumulation and coarse modes. Aerosol number and aerosol water are also calculated for each mode. Aerosol mass and number associated with stratiform cloud droplets are treated explicitly.

2.1 Marine aerosol source function

Size-resolved emissions of particle number, inorganic sea-salt, and OM mass from the surface ocean were calculated in CAM as functions of wind speed and surface ocean chlorophyll *a* (chl *a*) based on Long et al. (2011). Modeled size bins were centered on 0.039, 0.076, 0.15, 0.52, 2.4, 4.9, 15.1 and 30-µm diameters at 98 % relative humidity (i.e. RH within the laminar sub-layer immediately above the air-sea interface) across bin widths (dD_p) of 0.03, 0.05, 0.1, 0.2, 1.0, 3.0, 10.0 and 20.0 µm, respectively. Following dehydration to equilibrium water contents at an average RH of 80 % in the mixed layer above the laminar sub-layer, compositions were summed over the three aerosol size modes considered by CAM. Since the 3-mode version of CAM considers OM mass only

ACPD
13, 6067–6129, 2013

in the accumulation mode, the OM mass was summed over all particle sizes below 1.0-µm diameter at 80 % RH, and emitted directly into the accumulation mode (mode-1).

2.2 Prescribed conditions and initializations

CH_4, N_2O, and CO_2 mixing ratios were fixed at 1.77, 0.32, and 378 ppmv, respectively. O_3 was calculated online. Direct surface emissions of DMS, SO_2, secondary organic aerosol precursor gases, subgrid-scale NH_4HSO_4 (mode-1 and mode-2), NH_3, and NO_x were based on Dentener et al. (2006). Surface emissions of CO, CH_3OH, C_2H_4, C_3H_6, C_3H_8, and isoprene were based on the Precursors of Ozone and their Effects in the Troposphere (POET) database for 2000 (Granier et al., 2005).

The atmosphere model was initialized at 1 January 2000. Due to the heavy computational burden of running the MECCA mechanism, and to reduce model spin-up time, the sea-surface temperature was based on offline data for the 2000 calendar year, and was cycled annually. The sea-ice interface used version 4 of the Community Sea Ice Model (CSIM4; Briegleb et al., 2002). The land interface used version 2 of the Community Land Model (CLM2; Dickenson et al., 2006). Fields of chl *a* concentrations (in units of $mg\,m^{-3}$) in surface seawater were set equal to monthly averages derived from SeaWIFS imagery (1° × 1°, Gregg, 2008) for the period September 1997 through December 2002, as in Long et al. (2011). The aerosol modes were initialized at zero number with sizes centered log-normally on 0.026, 0.11, and 2.0 µm geometric mean dry diameters for the Aitken, accumulation, and coarse modes, respectively. The corresponding ranges for the log-normal centroids were 0.0087 to 0.052, 0.053 to 0.44, and 1.0 to 4.0 µm dry diameter respectively.

2.3 Global simulations and reporting conventions

Results for the coupled MECCA scheme, for which chemical reactions involving halogens were calculated explicitly (denoted *Hal*), were compared with corresponding runs for which halogen chemistry was turned off (denoted *NoHal*). Differences in results

ACPD
13, 6067–6129, 2013

were interpreted to evaluate the role of halogens in the physicochemical evolution of the atmosphere.

Unless otherwise stated, the following conventions are used. Values are based on grid-box area-weighted spatial fields for the simulated period from 1 January 2005–31 December 2014. Notation is specified for atmospheric region and time period over which statistics were calculated. Ten-year area-weighted statistics are referred to as ANN for annual, DJF for December/January/February, MAM for March/April/May, and JJA for June/July/August. Spatial statistics for specific atmospheric regions were compiled over the Northern and Southern Hemispheres, (NH and SH, respectively), the entire planetary boundary layer (PBL), the continental-only boundary layer (CBL), marine-only boundary layer (MBL), and the entire free troposphere (FT). Model layers corresponding to these regions are defined below. Analyses based on specific model layers (e.g. the surface layer) are specified as such. Results for a given atmospheric region are based on median and range of 10-yr mean climatology for that region and time period (as defined above). For example, the annual O_3 mixing ratio for the planetary boundary layer (ANN-PBL) would be reported as the median and range across the PBL of the 10-yr climatological mean.

Temporal-only statistics for a given grid box are reported as mean ± standard deviation. For example, a simulated mixing ratio corresponding to a long-term measurement site is reported only as a 10-yr climatological mean and standard deviation. When necessary to facilitate direct comparison with observations or results from other published simulations, simulated results are reported using the same convention as the reported values.

For all discussions here, the tropopause was defined as the minimum pressure level in the model (maximum altitude) above which the temperature lapse rate was positive between levels (70.06 mb or ~18 km), which is consistent with the World Meteorological Organization's tropopause definition. In CAM, the boundary layer is not well resolved, and was therefore defined as the lowest four levels (highest pressure) of the model atmosphere (below 867 mb). The free troposphere was defined as the region

ACPD
13, 6067–6129, 2013

between the top of the boundary layer and the tropopause. For comparisons with measurements at surface sites for which altitudes are known, simulated results were interpolated vertically to the corresponding measurement altitudes. Otherwise, the results from the likely nearest model pressure level were used. Unless otherwise noted, comparisons between results for *Hal* relative to *NoHal* simulations are presented as percent deviation defined as (using O_3 as an example),

$$\%\text{Deviation}(O_3) = \frac{[O_3]_{\text{Hal}} - [O_3]_{\text{NoHal}}}{[O_3]_{\text{NoHal}}} \times 100 \quad (1)$$

3 Results

3.1 Marine aerosol population characteristics

Mean aerosol composition and mixing ratios of gases simulated for each atmospheric region are compiled in the Supplement (Tables S1 through S6). Globally averaged annual marine aerosol production flux, burden, dry and wet deposition for both the *Hal* and *NoHal* (not shown, since these marine aerosol statistics were virtually identical for the simulated time period) simulations fell within the range of published estimates (Table 1). The total Na^+ mass flux was 25 % less than that reported by Long et al. (2011), which resulted in part from differences in model physics between the different CAM versions used in the two studies (3.5.07 for Long et al., 2011 and 3.6.33 here) and the number of aerosol size bins considered (8 for Long et al., 2011 and 3 here). The corresponding spatial range in mean Na^+ lifetimes against deposition was also within that reported by Pierce and Adams (2006) of 0.46 to 2.72 days. Mean dry deposition fluxes are towards the lower end of published estimates whereas wet fluxes fall near the mid-range of published estimates. Available evidence indicates that cloud and precipitation processes are represented reasonably well within CAM3 (e.g. Boville et al., 2006), which implies that simulated deposition fluxes are also reasonable.

ACPD
13, 6067–6129, 2013

3.2 Model sensitivity to inorganic halogen cycling

For the simulations reported herein, dehalogenation of marine aerosol is the only primary source for volatile inorganic Br and Cl species. Because emissions of halocarbons from marine biogenic sources, biomass- and fossil-fuel combustions, industrial sources, and terrestrial ecosystems, are not considered, the total global emissions of halogens correspond to lower limits. In addition, as discussed in detail by Keene et al. (2009), available evidence suggests that the MECCA scheme as currently configured overestimates rates of Br cycling to some extent and consequently, simulated rates of Br activation and associated impacts are considered upper limits. In the following text and tables, Br_t is defined as the sum of all volatile inorganic Br species and Cl^* is defined as all inorganic Cl gases other than HCl, which includes HOCl, $2 \times Cl_2$, $ClNO_2$, $ClNO_3$, OClO, and BrCl.

3.2.1 Br distributions

Simulated Br_t averaged over the tropospheric column ranged from 0.038 to 44 pmol mol^{-1} (median 6.1 pmol mol^{-1}). Median Br_t for ANN-FT was 2.5 (0.038 to 32) pmol mol^{-1}. von Glasow et al. (2004) reported Br_t from 1 to 6 pmol mol^{-1} for the FT based on simulations that considered Br sources other than sea-salt aerosol. While these ranges overlap, mixing ratios simulated by von Glasow (2004) are lower limits because the sources do not include marine aerosol production. Simulated zonal median Br_t reveals little Br_t in the upper troposphere and stratosphere, which is inconsistent with observation (e.g. Fitzenberger et al., 2000; see Supplement Fig. S1) and model calculations (von Glasow et al., 2004). Most stratospheric Br is believed to originate from the photolysis of long-lived organic Br species (e.g. CH_3Br) (Montzka et al., 2003), which are not considered in the MECCA chemical mechanism employed for these simulations or the emission fields for Modal-CAM. To achieve observed levels of stratospheric Br_t with the computational resources available for this analysis would have required offline Br sources. The radiative transfer scheme used to calculate

ACPD
13, 6067–6129, 2013

photochemical rates was tuned to reproduce stratospheric O_3 climatological means. Consequently, the impact of the upper-atmosphere Br on tropospheric photochemistry is believed to be negligible.

Global median vertical profiles and speciation of Br_t for ANN and JJA (Fig. 1) reveal that, between 700 to 800 mb pressure level (2 to 3 km altitude) and the surface, Br_t is dominated by roughly equal amounts of Br_2 and BrCl on a molecular basis. For DJF, BrCl was higher than Br_2 by a factor of about two. At higher altitudes, HBr (most of which is produced via the reaction of Br + HCHO) increases to become the dominant gas-phase Br species. In the lower troposphere, HBr is efficiently scavenged by liquid aerosol or cloud droplets. In the FT, most Br is recycled in the gas phase via

$$Br + O_3 \rightarrow BrO + O_2 \quad \text{(R1)}$$

$$BrO + h\nu \rightarrow Br + O(^3P) \quad \text{(R2)}$$

with an important secondary pathway (ranging from 5 % to 20 %) through

$$BrO + HO_2 \rightarrow HOBr + O_2 \quad \text{(R3)}$$

$$HOBr + h\nu \rightarrow Br + OH \quad \text{(R4)}$$

In the NH-FT, BrO + NO competes with R3 at approximately equal proportions. In the mid and high latitude FT of the NH and SH, 7 % to 15 % of HOBr is converted to BrCl via the multiphase pathway involving accumulation mode aerosol:

$$HOBr_{(g)} \rightarrow HOBr_{(aq)} \quad \text{(R5)}$$

$$HOBr_{(aq)} + Cl^- + H^+ \rightarrow BrCl_{(aq)} \quad \text{(R6)}$$

$$BrCl_{(aq)} \rightarrow BrCl_{(g)} \quad \text{(R7)}$$

In the MBL, 15 % to 50 % of HOBr reacts via the above pathway.

Multiphase recycling is not completely inactive in the FT. For example, a persistent but seasonally variable BrO maximum ranging from 3 to 4 pmol mol^{-1} was evident in the FT around 500 to 600 mb extending from approximately 60° S southward to the pole

ACPD
13, 6067–6129, 2013

(see BrO results below). This was driven by the condensation of HBr transported from the MBL across a band between 40° S to 20° S into the FT, southward, leading to the subsequent production (followed by volatilization and photolysis) of Br_2 via

$$HOBr_{(aq)} + Br^- + H^+ \rightarrow Br_{2(aq)} \quad \text{(R8)}$$

Reactions R1 through R4 and R5 through R7 complete the autocatalytic cycle. A recent paper by Roscoe et al. (2012) concluded that a large potential discrepancy between surface and remote-sensing measurements of BrO in Antarctica was resolved by a high abundance of BrO in the FT above the surface. This conclusion is supported by measured vertical profiles of BrO showing a maximum of nearly 9 pmol mol^{-1} at an altitude of 2 km (~ 700 to 800 mb). The general consistency between these observations and our moded results suggests that a significant amount of the BrO involved in chemistry over the Antarctic ice sheet is sea-salt derived. Further, McElroy et al. (1999) saw evidence for a high abundance of BrO in the Arctic FT that the authors were only able to conclude was driven by multiphase chemistry. While we cannot confirm that our results are indeed reflective of the true nature of these observations, they demonstrate a consistent regional-scale performance of our model's halogen cycling mechanism.

Measurements and model calculations indicate that, in the MBL, volatile inorganic Br typically has a relatively longer atmospheric lifetime against deposition than the parent marine aerosol (e.g. Sander et al., 2003; Keene et al., 2009). In addition, our model calculations indicate that significant amounts of relatively insoluble forms of Br_t are detrained from the MBL and accumulate in the FT whereas most of the highly soluble parent aerosol is largely confined to the MBL. Br cycling in the FT leads to enrichments in particulate Br relative to inorganic sea salt (i.e. EF(Br) > 1) throughout most of the FT (see Supplement Tables S1 and S2). Two pathways lead to accumulation of Br in aerosols: (1) in the FT, secondary Br^- is formed via the oxidation of aqueous SO_2 (in the form of HSO_3^- and SO_3^{2-}) by HOBr, and (2) the condensation of HBr onto newly formed and preexisting aerosol. The subsequent entrainment from the FT into the PBL of both Br-enriched aerosols and HBr, most of which subsequently condenses onto existing MBL aerosols, contributes to Br^- enrichments in the PBL. The role of this

ACPD
13, 6067–6129, 2013

dynamic process is evident in a slight but statistically significant ($p < 0.10$) negative correlation between HBr and model vertical velocity (not shown). The incorporation of secondary Br^- into fine-mode particles formed via nucleation, and subsequent coagulation into accumulation-mode particles likely affects EF(Br) across the size distribution, as well. However, since the model does not distinguish between fresh and aged aerosols, the relative contributions of different pathways to simulated EF(Br) in the PBL cannot be quantified explicitly.

Br enrichments in sub-µm fraction aerosol have been observed throughout the MBL (e.g. Sander et al., 2003) but until now models have been unable to explain them. In a CAABA box model, MECCA chemistry predicts efficient activation of particulate Br^- in all aerosol size fractions (e.g. Keene et al., 2009) and, thus, no significant Br enrichment of marine aerosol within the MBL. Our 3-D model calculations suggest that the detrainment of relatively insoluble forms of Br_t from the MBL into the FT, chemical processing within the FT, and the subsequent transport and entrainment of condensed or condensable reaction products back into the MBL accounts for the Br enrichment of sub-µm aerosol size fractions measured in the MBL. While Br is continuously cycled through the aerosol population even in low LWC environments, the equilibration with $HBr_{(g)}$ dominates the net Br exchange leading to steady state enrichments of the smaller (yet more abundant at altitude) aerosols. Both the zonal median EF(Br) for bulk aerosol in the model surface layer and available measurements of EF(Br) (taken from Sander et al., 2003) indicate a slight NH latitudinal gradient at high latitudes, which is more pronounced in the observations (Fig. 2). Sander et al. (2003) suggest that the EF(Br) greater than unity in the NH may result from anthropogenic Br emissions in the region (primarily the N. Sea and Scandinavia) leading to bulk enrichments. While zonal averages are not directly comparable to individual observations, the model suggests a stronger latitudinal trend in the SH. This is likely due to the strong subsidence in the high latitudes, consistent with the hypothesized mechanism of fine aerosol enrichment observed throughout the marine boundary layer. Sparse measurements in that region provide limited information with which to evaluate the simulated pattern. Geographically

ACPD
13, 6067–6129, 2013

and seasonally coincident comparisons between simulated and measured EF(Br) for size-resolved marine aerosol indicate strong agreement (Fig. 3g–i).

Comparison of simulated and observed Br_t reveals a fairly consistent pattern of model over-prediction. With the exception of the NE Atlantic adjacent to N. Africa, where the agreement was good, the model over-predicted Br_t by factors of 2 to 6 (Table 2). It is recognized that MECCA tends to overestimate Br_t as was the case in Keene et al. (2009) where simulated Br_t was high by a factor of about 3 relative to observations. It is important to note that, with the exception of Hawaii, the geographic locations in Table 2 were coincident with large gradients in NO_x and Br_t. The relatively coarse model resolution in these regions constrains the reliability of comparisons between observed and simulated values and probably contributes to the divergence in results.

Observations using the OMI instrument aboard NASA's Aura satellite are capable of constraining vertical abundances of BrO (reported as column abundances, cm^{-2}). It is difficult to partition observations into the contribution of BrO from different altitudes to the total column abundance. Vertically integrated simulated BrO (Fig. 4) ranged from 0.011×10^{13} to $4.9 \times 10^{13}\,cm^{-2}$ (consistent with von Glasow et al., 2004) over the simulated 10-yr annually averaged period. Median BrO column burdens were 0.56×10^{13}, 0.97×10^{13}, and $0.58 \times 10^{13}\,cm^{-2}$ for DJF, MAM, and JJA periods, respectively. Corresponding median PBL BrO mixing ratios were 1.1, 2.3 and $1.5\,pmol\,mol^{-1}$ for DJF, MAM and JJA, respectively. Median FT BrO was 0.15, 0.20 and $0.25\,pmol\,mol^{-1}$ for DJF, MAM and JJA, respectively. Maximum column integrated BrO for the MAM NH was $4.9 \times 10^{13}\,cm^{-2}$. An estimated tropospheric maximum column burden of $3.9\,(\pm 2.5) \times 10^{13}\,cm^{-2}$ was computed based on aircraft-based observed profiles (Salawitch et al., 2010). Typical NH spring-time peak total column burdens measured by satellite exceed our maximum values by a factor of ~ 2 (e.g. Richter et al., 2002). These peaks typically occur over the polar ice-caps and are believed to be due to "bromine explosions" during Arctic springtime (Simpson et al., 2007; Piot and von Glasow, 2008). While all hypothesized sources specific to the Arctic are not considered here, the results depicted in Fig. 4 provide a potentially useful background values for

ACPD
13, 6067–6129, 2013

estimating the contribution to total Br from sources other than activation pathways involving marine aerosol (e.g. reactions involving brine films on surfaces, frost flowers, organobromine precursors, downwelling of stratospheric BrO, etc.).

A subset of available measurements of BrO in the MBL is compared with the corresponding average values in Table 3. The model output mixing ratios are averaged over diel cycles. To estimate daytime mean mixing ratios from the diel averages, we assumed that BrO mixing ratios dropped to zero at night and adopted the fraction of hours of daylight appropriate for the time of year. Simulated daytime mixing ratios agreed with observations within a factor of about 2 to 3 at all locations. The simulated BrO maxima in the tropical Atlantic and Pacific MBL (Fig. 5b) have not been probed via direct measurement. But, as was the case with simulated Br_t, circulation and the coarse model resolution constrain the reliability of comparisons between measurements and simulated results in regions of strong chemical gradients. For example, mean BrO in grid boxes immediately to the east of that corresponding to Sao Vicente, Cape Verde were a factor of two lower than that reported in Table 3.

Throughout most of the lower troposphere and boundary layer, the BrO + NO reaction is the largest source of atomic Br (Table 4). The exception is the southern MBL where BrO + BrO, and HOBr and Br_2 photolysis dominate. In the global free troposphere simulated atomic Br originates primarily from BrO + NO and HOBr photolysis in approximately equal proportions. The dominant sources for simulated HOBr in the free troposphere are BrO + HO_2 (84 %) and BrO + CH_3O_2 (16 %; primarily from CH_4 oxidation). As the result of low liquid water content, Br radicals in the free troposphere recycle primarily in the gas phase; though as discussed above, heterogeneous recycling is also important.

3.2.2 Cl distributions

Simulated HCl mixing ratios are high in comparison with available measurements in the MBL. For example, Pszenny et al. (2003) measured HCl ranging from < 30 to 250 pmol mol^{-1} (mean, 100 pmol mol^{-1}) in on-shore flow within the Hawaiian MBL,

ACPD
13, 6067–6129, 2013

compared to a simulated surface median of 1247 (1046 to 1383) pmol mol^{-1}. The simulated values were driven by in situ acidification of marine aerosol by high volcanic SO_2 emissions which were emitted at the model surface. For comparison, simulated HCl upwind of the volcanic SO_2 plume was more than a factor of two lower. HCl measured along a transect in the E. Atlantic MBL was 682 (106 to 1404) pmol mol^{-1} in the vicinity of the European continent, 348 (91 to 746) pmol mol^{-1} adjacent to N. Africa, 82 (< 23 to 207) pmol mol^{-1} in the Intertropical Convergence Zone, and 267 (81 to 453) pmol mol^{-1} adjacent to S. Africa (Keene et al., 2009). Corresponding simulated median surface HCl mixing ratios for these regions were 352 (8 to 1577), 906 (271 to 1914), 424 (294 to 697), and 445 (0.11 to 3155) pmol mol^{-1}, respectively. Maximum HCl mixing ratios in the E. Atlantic were generally coincident with acid-displacement reactions involving HNO_3 in marine regions downwind of major NO_x emission sources. As for Br_t, the strong gradients along the cruise track constrain the reliability of comparisons between measured and simulated HCl.

Differences between aerosol pH in *Hal* versus *NoHal* simulations reflect the influence of HCl phase partitioning on aerosol solution acidity in the former versus lack thereof in the latter (not shown). Acid displacement of HCl by HNO_3 and other relatively more soluble acids transfers acidity from the aerosol solution to the gas phase and thereby sustains higher solution pHs in the *Hal* simulation (e.g. Keene et al., 1998). For all locations at which published estimates of aerosol pH based on in situ observations were available, simulated pHs based on *Hal* compared better with those estimates than did pHs based on *NoHal* (not shown; also see Keene et al., 2009).

Simulated Cl^* mixing ratios in the PBL are higher over much of the NH high-latitudes, relative to other regions, with peak values in marine-influenced air downwind of major population and industrial regions. This is due to interactions with high anthropogenic NO_x emissions (see Sect. 3.3.3). Simulated Cl^* in the SH-MBL (ranging from less than 0.01 to 340 pmol mol^{-1}, median 27 pmol mol^{-1}) was comprised of 46 %, 16 %, 6 % and 1 % BrCl, Cl_2 (on a molecular basis), HOCl, and $ClNO_2$, respectively, based on median values. Cl^* in the NH MBL was comprised of 20 %, 29 %, 3 % and 10 % BrCl, Cl_2, HOCl,

ACPD
13, 6067–6129, 2013

and $ClNO_2$, respectively, based on median values. In contrast, over NH continents, $ClNO_2$ made up 69 % of Cl^* and was higher than $ClNO_2$ in the NH-MBL by a factor of 10 (see Supplement Table S4). This reflects the differences in NO_x loadings between both continental and marine troposphere, and the Southern and Northern Hemispheres. In the MECCA chemical mechanism, $ClNO_2$ is produced at night and subsequently photolyzes following sunrise via

$$N_2O_5 + Cl^- \rightarrow ClNO_2 + NO_3^- \quad \text{(R9)}$$

$$ClNO_2 + h\nu \rightarrow Cl + NO_2; \quad \text{(R10)}$$

Significant production is limited to highly polluted conditions with NO_x mixing ratios greater than $\sim 1\,\mathrm{nmol\,mol^{-1}}$. There is some evidence of the importance of $ClNO_2$ cycling over coastal and continental regions (e.g. Ostoff et al., 2008; Simon et al., 2009; Thornton et al., 2010; Phillips et al., 2012). Mean simulated $ClNO_2$ mixing ratios in the summer time surface layer adjacent to the US Texas Gulf Coast were 134 ($\pm$51) $\mathrm{pmol\,mol^{-1}}$ and were consistent with both observations made by Osthoff et al. (2008) and non-polluted simulation results (Simon et al., 2009). Mean simulated $ClNO_2$ mixing ratios for February at Boulder, CO USA (40° N, 105° W) were 129 ($\pm$38) $\mathrm{pmol\,mol^{-1}}$, which is within the range of $ClNO_2$ mixing ratios observed by Thornton et al. (2010) in this region (ranging from less than 1 to 210 $\mathrm{pmol\,mol^{-1}}$). The simulated distribution of $ClNO_2$ over N. America (Fig. 6) is also generally consistent with production patterns based on the GEOS-Chem model (Thornton et al., 2010). $ClNO_2$ mixing ratios simulated by *Hal* are generally higher and extend over broader geographic regions downwind from continents relative those simulated by Erickson et al. (1999), and compare well with limited observations. During a March–April 2008 cruise in the North Atlantic, Kercher et al. (2009) report nighttime $ClNO_2$ mixing ratios from 100 to 250 $\mathrm{pmol\,mol^{-1}}$ within the Long Island sound (coordinates not reported; assumed in the vicinity of 41.5° N, 70° W), and at or near 25 to 50 $\mathrm{pmol\,mol^{-1}}$ further offshore (45° N, 55° W). Simulated $ClNO_2$ mixing ratios within the corresponding grid cells, adjusted by a factor of two to account for day length were 302 ($\pm$88.4) $\mathrm{pmol\,mol^{-1}}$ and

ACPD
13, 6067–6129, 2013

75.6 (±36.3) pmol mol^{-1}, respectively. The broad distribution of $ClNO_2$ in the high latitudes suggests that its transport and cycling is important as a source for atomic Cl and a nocturnal reservoir for NO_x in polluted continental and marine regions.

Simulated atomic Cl in the global MBL ranged from 0 to 8.4×10^4 cm^{-3}, which brackets reported values inferred from measurements of NMHCs and C_2Cl_4 (0 to $\sim 10^5$ cm^{-3}; Rudolph et al., 1996; Singh et al., 1996). The simulated atomic Cl concentration of $2.6 \pm 1.5 \times 10^4$ cm^{-3} in New England (USA) coast air during summer was within the corresponding range of estimates based on relative concentration changes in NMHCs (2×10^4 to 6×10^4 cm^{-3}; Pszenny et al., 2007). An estimate of $3.3 \pm 1.1 \times 10^4$ cm^{-3} derived from measurements made during a N. Atlantic cruise in June 1992 (Wingenter et al., 1996), was similar to a simulated value of $4.8 \pm 1.6 \times 10^4$ cm^{-3} for the same region. Measurements in the southern ocean MBL yielded estimated atomic Cl concentrations of 720 ± 100 cm^{-3} which is a factor of two lower than our simulated summertime surface mean of $2.0 \pm 1.6 \times 10^3$ cm^{-3} (Wingenter et al., 1999). The ANN-SH-MBL median for simulated values (3.5×10^3 cm^{-3}) was within the estimated 0.26×10^4 to 1.8×10^4 cm^{-3} required to sustain observed CH_4 isotope ratios in the southern MBL (Allan et al., 2001; Platt et al., 2004).

We note that, unless otherwise indicated, model output is based on monthly averages that do not reflect daytime maxima; and thus peak mixing ratios for species produced photochemically in ambient air are higher. In addition, the simulation did not consider non-marine sources for Cl in the atmosphere and thus the total production fluxes and burdens of Cl should be considered lower limits.

3.3 Impact of halogens on O_3, OH, HO_2 and NO_x

3.3.1 O_3

Deviations between the *Hal* and *NoHal* simulations of zonally averaged surface O_3 (Fig. 7) and the corresponding zonal-median vertical distribution fields (see

ACPD
13, 6067–6129, 2013

Supplement Fig. S3) reveal less O_3 globally in the *Hal* simulation. These results are driven primarily by (1) the direct destruction of O_3 via reaction with halogen radicals (Table 5) and (2) the net reduction in O_3 production resulting from the accelerated oxidation of NO_x via formation and processing of halogen nitrates (discussed in more detail below; Sander et al., 1999; Pszenny et al., 2004; Keene et al., 2009). The largest absolute deviations were in the high latitudes and generally coincident with relatively greater direct destruction of O_3 via reaction with atomic Br and NO (Fig. 7c). The reduction of NO_x and its influence on O_3 was also significant in the free troposphere with a similar latitudinal pattern (mean deviation of −39 %; not shown). These results are not consistent with those from previous studies in two respects. First, the geographic distribution of Br-mediated O_3 loss is different. Our simulation yields maximum impacts in high latitudes whereas other studies report that tropical regions are impacted to a greater degree (e.g. Yang et al., 2005; Saiz-Lopez et al., 2012). The causes for these differences are not entirely clear. In our study, the negative ozone deviations in high-latitude MBL and polar PBL are coincident with higher NO and lower HO_2 concentrations (see Sect. 3.3.2) relative to the *NoHal* simulations, which enhanced O_3 destruction via the $NO + O_3$ reaction path. In regions where NO abundance decreased from *NoHal* to *Hal* (e.g. in the remote tropical MBL) the net O_3 loss was also lower. Second, ozone loss is greater in our simulations. Saiz-Lopez et al. (2011) calculate net O_3 loss due to halogens from 6 to 20 % in the tropical troposphere. Our results exceed 20 % for most of the tropical MBL and are around 15 to 20 % for the tropical FT. It is not clear if Saiz-Lopez et al. (2012) also consider the indirect destruction of ozone via changes in HO_x/NO_x abundance and partitioning.

In addition, the suppression of RO_2 production by BrO leads to a net decrease in RO_2 mixing ratios in the PBL. This suppressed the reaction of $NO + RO_2$ globally by 38 % and 49 % in the PBL and FT, respectively, thereby contributing to net O_3 destruction.

O_3 simulated with *Hal* and *NoHal* is compared with O_3 measured in near surface air at Hawaii during September (Pszenny et al., 2004) and along a transect through the E.

ACPD
13, 6067–6129, 2013

Atlantic during October and November (Keene et al., 2009) in Fig. 9. In all cases, the *Hal* simulations yielded O_3 mixing ratios that were closer to those observed.

Annual mean O_3 mixing ratios for World Ozone and Ultraviolet Radiation Data Centre (WOUDC) sites (Table 6) are compared to corresponding simulated O_3 mixing ratios in the PBL and in the FT at the 500 mb pressure level in Fig. 10. Relative to mean mixing ratios measured in the PBL and 500 mb levels, deviations in mean (± standard deviation) O_3 simulated with *Hal* were −26 % (±21 %) and −27 % (±12 %), respectively. Corresponding deviations based on *NoHal* were 42 % (±25 %) and 9.3 % (±15 %), respectively. For the PBL, although the correlation coefficient for O_3 based on *NoHal* was higher, the *Hal* simulations better reproduce observed O_3 for nearly all stations (Fig. 10). Relative to *Hal*, or O_3 at the 500 mb level simulated with *NoHal* were closer to observed O_3 mixing ratios.

3.3.2 OH : HO_2

Median OH and HO_2 mixing ratios in the PBL simulated with *Hal* were lower by 41 % and 18 %, respectively, relative to *NoHal*. Differences were greatest in the MBL and resulted primarily from three processes. First, the enhancement of $NO + HO_2$ and the addition of $BrO + HO_2 \rightarrow HOBr + O_2$ (and subsequent uptake of HOBr by liquid aerosol) are HO_2 sinks. HOBr uptake by aerosols in the MBL was approximately equivalent to OH recycling via HOBr photolysis. Second, the accelerated rate of NO_2 oxidation by halogen species (Sect. 3.3.3) reduced the production of HO_2. In combination with increased NO in the vicinity of high HO_2 mixing ratios and lower O_3, this led to a net decrease in both OH and HO_2. Third, globally less O_3 reduced the photochemical production of $O(^1D)$. Overall, the OH : HO_2 ratio decreased 28 %, consistent with Keene et al. (2009) (3 % to 32 % decrease).

ACPD
13, 6067–6129, 2013

3.3.3 NO_x

The cycling of Cl and Br in the *Hal* simulations impacted distribution, speciation, and lifetimes of NO_x species in two ways. Under polluted conditions at night, N_2O_5 is produced from

$$NO_{2(g)} + O_{3(g)} \rightarrow NO_{3(g)} + O_{2(g)} \quad \text{(R11)}$$

$$NO_{3(g)} + NO_{2(g)} \leftrightarrow N_2O_{5(g)} \quad \text{(R12)}$$

Some N_2O_5 reacts with particulate Cl^- to produce $ClNO_2$ via R9. In addition, N_2O_5 also hydrolyzes to produce HNO_3, which accounts for 30 % to 50 % of the total NO_x sink in polluted regions (Alexander et al., 2009). The photolysis of $ClNO_2$ following sunrise via R10 regenerates half the NO_2 from which the precursor N_2O_5 was formed and also produces highly reactive Cl atoms. Thus, this pathway acts as both a source for halogen radicals and a nocturnal reservoir for NO_x that efficiently extends its atmospheric lifetime and thereby enhancing O_3 production relative to that predicted in the absence of R9 and R10 (as in *NoHal*). Figure 11a depicts the percent deviation of NO_x ($NO + NO_2$) in the PBL for *Hal* versus *NoHal* simulations. The increased NO_x lifetime resulting primarily from $ClNO_2$ production and processing is evident in the positive deviations along the primary transport pathways downwind of major pollution sources.

Under clearer conditions in the MBL, the formation and subsequent hydrolysis of halogen nitrates via

$$NO_2 + ClO \rightarrow ClNO_3 \quad \text{(R13)}$$

$$ClNO_3 + H_2O_{(l)} \rightarrow HOCl + HNO_3 \quad \text{(R14)}$$

and analogous reactions that produce $BrNO_3$ accelerates oxidation of NO_x (Sander et al., 1999; Pszenny et al., 2004; Keene et al., 2009). The influence of these reactions is evident in the negative deviations in NO_x simulated by *Hal* relative to *NoHal* for much of the global MBL (Fig. 11a) and in differences in median NO_x mixing ratios simulated with *Hal* versus *NoHal* for the NH MBL, SH MBL, and PBL. As noted above, the accelerated oxidation of NO_x via these pathways impacts oxidation processes through

ACPD
13, 6067–6129, 2013

net O_3 and OH destruction and modified OH/HO_2 ratios. In the Antarctic region, the presence of increased Br, and less O_3 and HO_x increased the lifetime of NO leading to a positive NO deviation while NO_2 decreases (Fig. 11b, c).

3.4 Impact of halogens on S cycling

In general, the global-scale sources, lifetimes, and sinks for major S species compare well with the modal-CAM standard chemical scheme and other global model studies of the S budget (Table 7). Major differences between MECCA and modal-CAM are driven in part by influences of halogens in the oxidation of DMS and SO_2, lower OH concentrations in the PBL in MECCA-CAM, and differences in the treatment of H_2SO_4.

The primary DMS oxidation pathways in the conventional mechanism considered in most models are reaction with OH during daytime and reaction with NO_3 at night. DMS burden and lifetime in *NoHal* are about five times that in the standard modal-CAM, due to lower OH and NO_3 concentrations (factor of 2 to 3 for both) in the global PBL. The *Hal* and *NoHal* simulations calculate OH online while standard modal-CAM uses an offline oxidant database of monthly averages taken from simulations by a chemistry-climate model (Lamarque et al., 2010).

Oxidation of DMS by BrO has been proposed as an important alternate pathway (Toumi, 1994; von Glasow, 2002) and oxidation by atomic Cl may also be significant at high Cl-atom concentrations (Keene et al., 1996). Comparison of the major DMS reaction pathways is presented in Table 8. *Hal* simulations indicate that reaction with BrO is important throughout the whole atmosphere, and responsible for 84 % of all DMS oxidation in the Southern Hemisphere MBL. Comparing the total oxidation rate shows that DMS is oxidized faster globally (Table 8, factor of 1.40 in the PBL) than would be predicted by the reaction with OH and NO_3 alone. Globally, median DMS mixing ratios were lower by 74 % and 89 % in the PBL and FT, respectively. The greatest differences in DMS mixing ratios were coincident with emissions patterns in the SH MBL (Fig. 13c), reflecting the faster oxidation in the *Hal* simulations. Positive DMS deviations were coincident with low relative mixing ratios.

ACPD
13, 6067–6129, 2013

The SO_2 budgets for the *Hal* and *NoHal* simulations are quite similar. In comparison to the standard modal-CAM, the main difference is the lower gas-phase oxidation due to lower PBL OH concentration in MECCA-CAM, and slower aqueous uptake. In both *Hal* and *NoHal* simulations, oxidation by H_2O_2 in the cloud water aqueous phase was the single most important sink for SO_2 globally (Table 8). In the *Hal* simulation, oxidation of S(IV) in deliquesced aerosols accounted for about 12 % of S(IV) oxidation in the SH MBL, but only 1 % globally. Aqueous-phase pathways for S(IV) oxidation in aerosol solutions are strongly pH dependent (Chameides and Stelson, 1992; Keene et al., 1998). For size fractions that overlap, simulated aerosol pH's based on *Hal* are reasonably representative of available estimates inferred from direct measurements (Fig. 3). The mediation of pH by acid-displacement in the *Hal* simulation resulted in a much greater uptake of SO_2 in aerosol (Fig. 13b). $SO_{2(g)}$ and aerosol S(IV) simulated for the ANN-PBL by *Hal* versus *NoHal* (Fig. 13a, b) diverged by median values of −7.73 % (−77.4 % to 686 %) and 428 % (−99.9 % to 1.87×10^7 %), respectively. These differences are driven primarily by the absence of acid-displacement reactions involving HCl and the associated low aerosol solution pHs (by 1 to 2 units) in *NoHal*. Significant aqueous-phase oxidation of S(IV) by O_3 in aerosol solutions is limited to alkaline conditions (Chameides and Stelson, 1992) and, consequently, this pathway was important only in the SH where persistent high winds sustain high concentrations of marine aerosol (Long et al., 2011), sources of acidity are relatively low, and, thus pH values are relatively high (see Tables S1 and S2). The lower pH of aerosol solutions in other regions efficiently suppressed aerosol S(IV) oxidation by O_3 in *Hal* simulations (Table 8). Aqueous-phase oxidation of S(IV) by HOCl and HOBr enhances production of S(VI) in moderately acidic (pH 5 to 6 aerosol solutions; Vogt et al., 1996; Keene et al., 1998; von Glasow et al., 2002) but production via these pathways decreases with decreasing pH due to the lower solubility of SO_2 (Keene et al., 2009). As noted above, aerosol pH values simulated by *Hal* are reasonably consistent with those derived from observations. The pH range of 5 to 6 is transient and, in most regions, acidified aerosols rapidly equilibrate with atmospheric acids at somewhat lower pHs. Consequently, *Hal*

ACPD
13, 6067–6129, 2013

simulations indicate oxidation of S(IV) by hypohalous acids accounts for minor to negligible fractions of S(IV) oxidation in the MBL globally (Table 8). Differences in our results compared to von Glasow et al. (2002) were due to the inability to differentiate between cloudy and non-cloudy conditions in our monthly-mean model datasets, whereas von Glasow et al. (2002) were able to explicitly differentiate processes under clear-sky and cloudy conditions.

The most noticeable budget differences between CAM/MECCA and the standard modal-CAM are for H_2SO_4 vapor. In *Hal* and *NoHal*, the H_2SO_4 source (from SO_2 reaction with OH) is smaller but the burden and lifetime are higher, which was driven by several factors. First, the lower PBL OH concentrations in *Hal* and *NoHal* result in more SO_2 being mixed into the FT where the total aerosol surface area and liquid water content are low and $H_2SO_{4(g)}$ loss by condensation is relatively slow resulting in higher burdens and lifetimes. Modal-CAM calculates H_2SO_4 vapor production (by gas-phase chemistry) and uptake by aerosols sequentially, while *Hal* and *NoHal* calculate them simultaneously, which has been shown to affect H_2SO_4 vapor concentrations (Kokkola et al., 2009). In addition, modal-CAM uses the Fuchs–Sutugin equation to calculate H_2SO_4 mass-transfer rates from gas to particle phases, whereas *Hal* and *NoHal* use the method of Schwartz (1986), yielding mass-transfer rates generally slower in *Hal* and *NoHal* than in modal-CAM (Sander, 1999). A more detailed evaluation of differences in the simulated H_2SO_4 vapor concentrations is beyond the scope of this study. The higher $H_2SO_{4(g)}$ concentrations in the FT also lead to higher rates of nucleation and growth of new particles in *Hal* and *NoHal*. Particle number concentrations based on enhanced nucleation in *Hal* yielded reasonably good agreement with observations from a wide range of locations (Table 9), while other studies report underestimations of concentrations under similar conditions (Adams and Seinfeld, 2002; Spracklen et al., 2005). These differences are important to aerosol microphysics in the FT, and thus deserve further investigation. However, they do not significantly impact the budget or distribution of nss-SO_4^{2-} in the simulations.

ACPD
13, 6067–6129, 2013

The global nss-SO_4^{2-} budgets for *Hal* and *NoHal* were nearly indistinguishable, while compared to a 5-yr simulation of the standard modal-CAM, the nss-SO_4^{2-} burden and lifetimes were 30 % to 40 % higher (Table 7). Globally, nss-SO_4^{2-} shifted to smaller size bins driven by transport and subsequent oxidation of SO_2 from the PBL into the FT in the CAM-MECCA system versus standard modal-CAM. While the *Hal* and *NoHal* global S budgets are close, there are regional differences approaching ± 30 % for PBL concentrations. In the NH PBL, nss-SO_4^{2-} was generally higher in *Hal* (Fig. 12d) due to enhanced gas-phase and aqueous-aerosol oxidation of SO_2 (Fig. 12b), less oxidation in cloud droplets, and the shorter lifetime of nss-SO_4^{2-} produced in cloud droplets. Lower nss-SO_4^{2-} in the Indian and SE Asian PBL was driven in part by an ∼ 10 % increase rain and wet removal. Effects of interactions between chemistry, weather and climate will be addressed in a subsequent paper. The largest relative (Fig. 12d) and absolute (not shown) nss-SO_4^{2-} positive deviations occurred immediately downwind of large anthropogenic sources of SO_2 in eastern China and the eastern USA. This was due to higher aerosol pH leading to more SO_2 uptake (Fig. 12a, b). Directly further upwind from these nss-SO_4^{2-} deviation maxima, aqueous S(IV) deviations become negative, indicating enhanced oxidation of S(IV) by aqueous halogen radicals (HOCl and HOBr). In addition, a significant positive global correlation between nss-SO_4^{2-} and aerosol liquid water ($R^2 = 0.55$; $p < 0.01$) in the PBL suggests a non-linear positive feedback link between aerosol hygroscopicity and its ability to take up and oxidize SO_2 in the aqueous phase. In the SH, the nss-SO_4^{2-} burden decreased by 19 % on average, due to faster gas-phase oxidation of DMS (primarily by BrO) and somewhat lower yield of SO_2, more efficient uptake of SO_2 in larger aerosol particles with higher pH, and faster deposition of the nss-SO_4^{2-} formed in the larger particles (see Tables 7 and 8). Based on comparisons with observations, *Hal* and *NoHal* provided similar resolution in predicting mean annual SO_2 and nss-SO_4^{2-} (Fig. 13, Table 10).

Relative to the conventional pathways considered in *NoHal* and most other models, the net global effects of halogen chemistry on S cycling in marine air are accelerated

ACPD
13, 6067–6129, 2013

oxidation of DMS thereby reducing its atmospheric lifetime. Despite relatively large influences on some pathways in the marine S cycle (Table 7), the domination of S cycling by continental and anthropogenically influenced air masses (where halogen chemistry is relatively less important) and by non-halogen aqueous chemistry in clouds limited the overall net effect of halogens on the atmospheric S budget. However, simulated results suggest potential non-linear feedbacks that may significantly alter nss-SO_4^{2-} distributions downwind of major sources.

3.5 Halogen interactions NMHC, CH_4

The oxidation of CH_4 and NMHC's is the primary source of O_3 in the troposphere through the production of organic peroxy-radicals that short-circuit the destruction of O_3 by NO. Relative to the *NoHal*, reactions involving halogens in *Hal* decreased the total rate of CH_3O_2 formation by 9 % and 13 % in the PBL and FT, respectively, and total CH_3O_2 destruction by 2 % and 14 % in the PBL and FT, respectively. These reactions resulted in lower steady-state mixing ratios of CH_3O_2 throughout most of the global troposphere (not shown). CH_3O_2 in the FT did not vary significantly between the two runs.

Averaged globally, in combination with lower OH plus reaction with atomic Cl, CH_4 oxidation rates decreased by 3 % relative to the *NoHal* simulation. The corresponding oxidation rates in the continental and marine boundary layer were higher by 13 % and 9 %, respectively, reflecting the production of atomic Cl in the lower atmosphere. While atomic Cl mixing ratios were comparable to (sparse) inferred observations, simulated CH_4 mixing ratios were fixed throughout the atmosphere. As such, these results are considered upper limits.

ACPD
13, 6067–6129, 2013

4 Discussion

The study presented here compared simulated multiphase chemistry of the atmosphere based on chemical reactions involving inorganic Cl and Br. Comparisons between the *Hal* and *NoHal* simulations demonstrate that a multiphase chemical mechanism is capable of reproducing major, and in some cases previously unresolved, characteristics of the aerosol and gas-phase chemical composition of the atmosphere including gas-phase Cl and Br species and aerosol pH. Further, this work suggests that much of the observed distribution and impact of halogens and related chemical cycling in the PBL and lower FT may be explained with sea-salt derived Cl and Br alone. Results also highlight the role of meteorology and circulation in observations of reactive halogens and aerosol composition. The reproduction of observed EF(Br) and EF(Cl), and the model's dependence upon interactions between the FT and PBL in the enrichment process strongly suggests (1) that halogen cycling is important in the FT, (2) that FT halogen cycling is tightly coupled with PBL chemistry, and (3) global-scale circulation and dynamics play a large role in the global distribution, partitioning and impacts of inorganic Cl and Br species. The results also suggest that SO_2 oxidation by HOBr and HOCl primarily in the FT plays a central role in this dynamic connection.

Comparison with observations indicate the *Hal* simulations reproduced tropospheric O_3 in the MBL with reasonable confidence, and that systematic biases in O_3 simulated with conventional chemical schemes were directly and indirectly attributable to reactions involving halogens. Reactions involving halogens destroyed significant quantities of O_3 throughout the MBL and the global troposphere. These pathways included direct destruction via reaction with halogen radicals and the accelerated regional oxidation of NO_x via the formation and processing of halogen nitrates. *Hal* simulations indicate that the formation and processing of $ClNO_2$ in the polluted NH PBL increases the atmospheric lifetime and transport of NO_x, alters NO/NO_2 partitioning; and activates significant atomic Cl with associated implication for oxidation processes.

ACPD
13, 6067–6129, 2013

Nss-SO_4^{2-} lifetimes were extended immediately downwind of major sources of SO_2 due to the enhanced uptake of SO_2 by higher pH aerosol in the *Hal* simulation versus *NoHal*. The oxidation DMS and to a lesser extent S(IV) by halogens in the MBL significantly modified regional S cycling relative to that based on conventional chemical pathways considered in most models. DMS oxidation was enhanced by the reaction with BrO and Cl, accounting for 60 % of DMS oxidation throughout the entire troposphere. In the *Hal* simulation, reactions in aqueous aerosol particles accounted for 12 % of the total S(IV) oxidation in the SH MBL, but only about 1 % globally. Reaction with HOCl and HOBr in moderately acidic aerosol solutions increased S(IV) oxidation rates in the PBL by only 1.2 %. Overall, halogen chemistry increased rates of S(VI) production from precursors.

Systematic differences in Br_t and Br species suggest a high sensitivity of the chemical system driven by these simulations to multiphase exchange of soluble gas-phase species. It is important to note that published values of Henry's Law constants (K_H) of several species governing gas/aerosol partitioning vary by large amounts. Published values K_H's for Br_2, BrCl and HBr all vary by factors of two or greater (see http://www.henrys-law.org for a detailed discussion and compilation of Henry's Law constants).

Major influences of halogen cycling on radiation, precipitation, and related climate processes will be evaluated in detail in a follow-up manuscript. The results presented here have important implications for feedbacks between the atmospheric chemistry and climate system and anthropogenically forced changes in atmospheric composition. The continued expansion of the human population and global-scale industrialization will certainly result in increased emissions of acids and acid precursors. The results herein suggest that throughout most of the unpolluted Southern Hemisphere, halogen radical chemistry is already important. The increased acidification of marine aerosol in this region would lead to increased activation of halogen species with associated implications. It has been hypothesized that, at pH levels observed in the remote marine atmosphere, modest increases in acidity in this region would yield disproportionately

ACPD
13, 6067–6129, 2013

large increases in Cl and Br activation rates (Sander et al., 2003). This study suggests that large-scale changes in halogen activation at the surface would impact the entire troposphere. The long-term implications of increased activation, though, cannot be assessed in the with short-term simulation studies such as this.

In addition, current projections indicate that climate change will alter global and regional wind fields. Since marine aerosol production scales exponentially with wind speed, such changes would have major consequences for the production, atmospheric concentrations, and processing of marine aerosol. Although the feedbacks cannot be assessed directly from this study, our results suggest that they would be significant. For example, in most regions, the larger size fractions that dominate production fluxes of marine aerosol mass are significantly debrominated during their atmospheric lifetime (e.g. Keene et al., 2009). Consequently, in MBL regions with sufficient acidity to titrate marine-derived alkalinity, available evidence suggests that enhanced wind-driven production of marine aerosols will lead to more vigorous Br-radical chemistry and associated feedbacks on tropospheric composition. Lastly, inorganic Br is believed to be a primary Hg oxidant in the atmosphere and may control Hg's atmospheric lifetime and deposition (Holmes et al., 2010). Large-scale emission of Hg to the atmosphere in South America associated with artisanal gold mining, combined with the potential for accelerated release of reactive Br into the Southern Hemisphere due to industrialization could pose a significant regional- to global-scale hazard.

Future research to address these issues would require the capacity to run century-scale simulations using a fully-coupled (with an ocean model) configuration. To this end, the computational limitations of the system used here are prohibitively large. Additional effort is needed to increase the efficiency of the chemical solution and improve the capacity to store data.

Still, several immediate research questions are apparent. Available evidence suggests that the production and processing of some compounds that are not considered in the current chemical mechanism are or may be important in atmospheric chemistry. These include (1) organic Cl^- and Br^- containing compounds that are hypothesized to

ACPD
13, 6067–6129, 2013

be the major sources of halogen radicals to the upper troposphere and stratosphere (see Sander et al., 2003 and references therein) and (2) iodocarbons and perhaps I_2 that are emitted from the ocean surface and significantly impact photochemistry and redox cycles in the MBL (Read et al., 2008; Saiz-Lopez et al., 2011). Finally, large uncertainties in the parameterization of transfer coefficients and thermodynamic properties of some compounds (e.g. Henry's Law constants for Br species) must be resolved to improve our current understanding of and ability to reliably simulate multiphase processes.

Supplementary material related to this article is available online at: http://www.atmos-chem-phys-discuss.net/13/6067/2013/acpd-13-6067-2013-supplement.pdf.

Acknowledgements. Financial support was provided by the US Department of Energy's (DOE's) Office of Science through the Office of Biological and Environmental Research (BER, grant numbers DE-FG02-07ER64442 and DE-SC0007120 to the University of Virginia), a Global Change Education Program Graduate Research Environmental Fellowship, and the National Center for Computational Sciences at Oak Ridge National Laboratory, which is supported by DOE's Office of Science (BER) under Contract DE-AC05-00OR22725. The CESM project is supported by the National Science Foundation and the DOE's Office of Science (BER). PNNL authors were funded by the US Department of Energy, Office of Science, Scientific Discovery through Advanced Computing (SciDAC) Program. The Pacific Northwest National Laboratory is operated for DOE by Battelle Memorial Institute under contract DE-AC06-76RLO 1830.

ACPD
13, 6067–6129, 2013

References

Adams, P. J. and Seinfeld, J. H.: Predicting global aerosol size distributions in general circulation models, J. Geophys. Res., 107, 4370, doi:10.1029/2001JD001010, 2002.

Alexander, B., Hastings, M. G., Allman, D. J., Dachs, J., Thornton, J. A., and Kunasek, S. A.: Quantifying atmospheric nitrate formation pathways based on a global model of the oxygen isotopic composition ($\Delta^{17}O$) of atmospheric nitrate, Atmos. Chem. Phys., 9, 5043–5056, doi:10.5194/acp-9-5043-2009, 2009.

Allan, W., Lowe, D. C., and Cainey, J. M.: Active chlorine in the remote marine boundary layer: modeling anomalous measurements of $d^{13}C$ in methane, Geophys. Res. Lett., 28, 3239–3242, 2011.

Anastasio, C. and Newberg, J. T.: Sources and sinks of hydroxyl radical in sea-salt particles, J. Geophys. Res., 112, D10306, doi:10.1029/2006JD008061, 2007.

Andreae, M. O. and Rosenfeld, D.: Aerosol-cloud-precipitation interactions. Part 1. The nature and sources of cloud-active aerosols, Earth Sci. Rev., 89, 13–41, 2008.

Birmili, W., Wiedensohler, A., Heintzenberg, J., and Lehmann, K.: Atmospheric particle number size distribution in central Europe: statistical relations to air masses and meteorology, J. Geophys. Res.-Atmos., 106, 32005–32018, 2001.

Boville, B. A., Rasch, P. J., Hack, J. J., and McCaa, J. R.: Representation of clouds and precipitation processes in the Community Atmosphere Model Version 3 (CAM3), J. Climate, 19, 2184–2198, 2006.

Briegleb, B. P., Hunke, E. C., Bitz, C. M., Lipscomb, W. H., Holland, M. M., Schramm, J. L., and Moritz, R. E.: The sea ice simulation of the Community Climate System Model, version 2, Tech Rep no. NCAR-TN-455, Nat. Center for Atm. Res., Boulder, CO, 34 pp., 2004.

Chameides, W. L. and Stelson, A. W.: Aqueous-phase chemical processes in deliquescent sea-salt aerosols: a mechanism that couples the atmospheric cycles of S and sea salt, J. Geophys. Res., 97, 20565–20580, 1992.

Clarke, A. D., Owens, S. R., and Zhou, J.: An ultrafine sea salt flux from breaking waves: implications for cloud condensation nuclei in the remote marine atmosphere, J. Geophys. Res., 111, D06202, doi:10.1029/2005JD006565, 2006.

Dentener, F., Kinne, S., Bond, T., Boucher, O., Cofala, J., Generoso, S., Ginoux, P., Gong, S., Hoelzemann, J. J., Ito, A., Marelli, L., Penner, J. E., Putaud, J.-P., Textor, C., Schulz, M., van der Werf, G. R., and Wilson, J.: Emissions of primary aerosol and precursor gases in

ACPD
13, 6067–6129, 2013

the years 2000 and 1750 prescribed data-sets for AeroCom, Atmos. Chem. Phys., 6, 4321–4344, doi:10.5194/acp-6-4321-2006, 2006.
Dickerson, R. R., Rhoads, K. P., Carsey, T. P., Oltmans, S. J., Burrows, J. P., and Crutzen, P. J.: Ozone in the remote marine boundary layer: a possible role for halogens, J. Geophys. Res., 104, 21385–21395, 1999.
Dickinson, R. E., Oleson, K. W., Bonan, G. B., Hoffman, F., Thornton, P., Vertenstein, M., Yang, Z.-L., and Zeng, X.: The Community Land Model and it's climate statistics as a component of the Community Climate System Model, J. Climate, 19, 2302–2324, 2006.
Erickson III, D. J., Seuzaret, C., Keene, W. C., and Gong, S. L.: A general circulation model based calculation of HCl and $ClNO_2$ production from sea salt dechlorination: reactive chlorine emissions inventory, J. Geophys. Res., 104, 8347–8372, doi:10.1029/98JD01384, 1999.
Fitzenberger, R., Bösch, H., Camy-Peyret, C., Chipperfield, M. P., Harder, H., Platt, U., Sinnhuber, B.-M., Wagner, T., and Pfeilsticker, K.: First profile measurements of tropospheric BrO, Geophys. Res. Lett., 27, 2921–2924, 2000.
Galbally, I. E., Bentley, S. T., and Meyer, C. P.: Mid-latitude marine boundary-layer ozone destruction at visible sunrise observed at Cape Grim, Tasmania, Geophys. Res. Lett., 27, 3841–3844, 2000.
Gent, P. R., Yeager, S. G., Neale, R. B., Levis, S., and Bailey, D. A.: Improvements in a half degree atmosphere/land version of the CCSM, Clim. Dynam., 34, 819–833, doi:10.1007/s00382-009-0614-8, 2009.
Granier, C., Guenther, A., Lamarque, J., Mieville, A., Müller, J., Olivier, J., Orlando, J., Peters, J., Petron, G., Tyndall, G., and Wallens, S.: POET, a database of surface emissions of ozone precursors, available at: http://www.aero.jussieu.fr/projet/ACCENT/POET.php, 2005.
Gregg, W. W.: Assimilation of SeaWIFS global ocean chlorophyll data into a three-dimensional global ocean model, J. Marine Syst., 69, 205–225, 2008.
Holmes, C. D., Jacob, D. J., Corbitt, E. S., Mao, J., Yang, X., Talbot, R., and Slemr, F.: Global atmospheric model for mercury including oxidation by bromine atoms, Atmos. Chem. Phys., 10, 12037–12057, doi:10.5194/acp-10-12037-2010, 2010.
Kamra, A. K., Murugavel, P., and Pawar, S. D.: Measured size distributions of aerosols over the Indian Ocean during INDOEX, J. Geophys. Res., 108, 8000, doi:10.1029/2002JD002200, 2003.
Keene, W. C., Jacob, D. J., and Fan, S. M.: Reactive chlorine: a potential sink for dimethylsulfide and hydrocarbons in the marine boundary layer, Atmos. Environ., 30, 6, i–iii, 1996.

ACPD
13, 6067–6129, 2013

Keene, W. C., Sander, R., Pszenny, A. A. P., Vogt, R., Crutzen, P. J., and Galloway, J. N.: Aerosol pH in the marine boundary layer: a review and model evaluation, J. Aerosol Sci., 29, 339–356, 1998.

Keene, W. C., Stutz, J., Pszenny, A. A. P., Maben, J. R., Fischer, E., Smith, A. M., von Glasow, R., Pechtl, S., Sive, B. C., and Varner, R. K.: Inorganic chlorine and bromine in coastal New England air during summer, J. Geophys. Res., 112, D10S12, doi:10.1029/2006JD007689, 2007.

Keene, W. C., Long, M. S., Pszenny, A. A. P., Sander, R., Maben, J. R., Wall, A. J., O'Halloran, T. L., Kerkweg, A., Fischer, E. V., and Schrems, O.: Latitudinal variation in the multiphase chemical processing of inorganic halogens and related species over the eastern North and South Atlantic Oceans, Atmos. Chem. Phys., 9, 7361–7385, doi:10.5194/acp-9-7361-2009, 2009.

Kercher, J. P., Riedel, T. P., and Thornton, J. A.: Chlorine activation by N_2O_5: simultaneous, in situ detection of $ClNO_2$ and N_2O_5 by chemical ionization mass spectrometry, Atmos. Meas. Tech., 2, 193–204, doi:10.5194/amt-2-193-2009, 2009.

Kerkweg, A., Sander, R., Tost, H., Jöckel, P., and Lelieveld, J.: Technical Note: Simulation of detailed aerosol chemistry on the global scale using MECCA-AERO, Atmos. Chem. Phys., 7, 2973–2985, doi:10.5194/acp-7-2973-2007, 2007.

Kerkweg, A., Jöckel, P., Pozzer, A., Tost, H., Sander, R., Schulz, M., Stier, P., Vignati, E., Wilson, J., and Lelieveld, J.: Consistent simulation of bromine chemistry from the marine boundary layer to the stratosphere – Part 1: Model description, sea salt aerosols and pH, Atmos. Chem. Phys., 8, 5899–5917, doi:10.5194/acp-8-5899-2008, 2008.

Kokkola, H., Hommel, R., Kazil, J., Niemeier, U., Partanen, A.-I., Feichter, J., and Timmreck, C.: Aerosol microphysics modules in the framework of the ECHAM5 climate model – intercomparison under stratospheric conditions, Geosci. Model Dev., 2, 97–112, doi:10.5194/gmd-2-97-2009, 2009.

Lamarque, J.-F., Bond, T. C., Eyring, V., Granier, C., Heil, A., Klimont, Z., Lee, D., Liousse, C., Mieville, A., Owen, B., Schultz, M. G., Shindell, D., Smith, S. J., Stehfest, E., Van Aardenne, J., Cooper, O. R., Kainuma, M., Mahowald, N., McConnell, J. R., Naik, V., Riahi, K., and van Vuuren, D. P.: Historical (1850–2000) gridded anthropogenic and biomass burning emissions of reactive gases and aerosols: methodology and application, Atmos. Chem. Phys., 10, 7017–7039, doi:10.5194/acp-10-7017-2010, 2010.

ACPD
13, 6067–6129, 2013

Lawler, M. J., Finley, B. D., Keene, W. C., Pszenny, A. A. P., Read, K. A., von Glasow, R., and Saltzman, E. S.: Pollution-enhanced reactive chlorine chemistry in the eastern tropical Atlantic boundary layer, Geophys. Res. Lett., 36, L08810, doi:10.1029/2008GL036666, 2009.

Leitte, A. M., Schlink, U., Herbarth, O., Wiedensohler, A., Pan, X., Hu, M., Richter, M., Wehner, B., Tuch, T., Wu, Z., Yang, M., Liu, L., Breitner, B., Cyrys, J., Peters, A., Wichmann, H., and Franck, U.: Size-segregated particle number concentrations and respiratory emergency room visits in Beijing, China, Environ. Health Persp., 119, 508–513, 2011.

Liu, X., Easter, R. C., Ghan, S. J., Zaveri, R., Rasch, P., Shi, X., Lamarque, J.-F., Gettelman, A., Morrison, H., Vitt, F., Conley, A., Park, S., Neale, R., Hannay, C., Ekman, A. M. L., Hess, P., Mahowald, N., Collins, W., Iacono, M. J., Bretherton, C. S., Flanner, M. G., and Mitchell, D.: Toward a minimal representation of aerosols in climate models: description and evaluation in the Community Atmosphere Model CAM5, Geosci. Model Dev., 5, 709–739, doi:10.5194/gmd-5-709-2012, 2012.

Long, M. S., Keene, W. C., Kieber, D. J., Erickson, D. J., and Maring, H.: A sea-state based source function for size- and composition-resolved marine aerosol production, Atmos. Chem. Phys., 11, 1203–1216, doi:10.5194/acp-11-1203-2011, 2011.

Long, M. S., Keene, W. C., Easter, R., Sander, R., Kerkweg, A., Erickson, D., Liu, X., and Ghan, S.: Implementation of the chemistry module MECCA (v2.5) in the modal aerosol version of the Community Atmosphere Model component (v3.6.33) of the Community Earth System Model, Geosci. Model Dev., 6, 255–262, doi:10.5194/gmd-6-255-2013, 2013.

Mårtensson, E. M., Nilsson, E. D., deLeeuw, G., Cohen, L. H., and Hansson, H.-C.: Laboratory simulations and parameterization of the primary marine aerosol production, J. Geophys. Res., 108, 4297, doi:10.1029/2002JD002263, 2003.

Mäkelä J. M., Koponen, I. K., Aalto, P., and Kulmala, M.: One-year data of submicron size modes of tropospheric background aerosol in southern Finland, J. Aerosol Sci., 31, 595–611, 2000.

McDow, S. R., Jang, M., Hong, Y., and Kamens R. M.: An approach to studying the effects of organic composition on atmospheric aerosol photochemistry, J. Geophys. Res., 101, 19593–19600, 1996.

McElroy, C. T., McLinden, C. A., and McConnell, J. C.: Evidence for bromine monoxide in the free troposphere during the Arctic polar sunrise, Nature, 397, 338–340, 1999.

Monahan, E. C. and O'muircheartaigh, I. G.: Whitecaps and the passive remote-sensing of the ocean surface, Int. J. Remote Sens., 7, 627–642, 1986.

ACPD
13, 6067–6129, 2013

Montzka, S. A., Butler, J. H., Hall, B. D., Mondeel, D. J., and Elkins, J. W.: A decline in tropospheric organic bromine, Geophys. Res. Lett., 30, 1826, doi:10.1029/2003GL017745, 2003.
Nagao I., Matsumoto, K., and Tanaka, H.: Sunrise ozone destruction found in the sub-tropical marine boundary layer, Geophys. Res. Lett., 26, 3377–3380, 1999.
O'Dowd, C. D. and Smith, M. H.: Physico-chemical properties of aerosol over the North East Atlantic: evidence for wind speed related sub-micron sea-salt aerosol production, J. Geophys. Res., 98, 1137–1149, 1993.
O'Dowd, C. D., Smith, M. H., Consterdine, I. E., and Lowe, J. A.: Marine aerosol, sea-salt, and the marine sulphur cycle: a short review, Atmos. Environ., 31, 73–80, 1997.
Osthoff, H. D., Roberts, J. M., Ravishankara, A. R., Williams, E. J., Lerner, B. M., Sommariva, R., Bates, T. M., Coffman, D., Quinn, P. K., Dibb, J. E., Stark, H., Burkholder, J. B., Talukdar, R. K., Meagher, J., Fehsenfeld, F. C., and Brown, S. S.: High levels of nitryl chloride in the polluted subtropical marine boundary layer, Nat. Geosci., 1, 324–328, doi:10.1038/ngeo177, 2008.
Phillips, G. J., Tang, M. J., Thieser, J., Brickwedde, B., Schuster, G., Bohn, B., Lelieveld, J., and Crowley, J. N.: Significant concentrations of nitryl chloride observed in rural continental Europe associated with the influence of sea salt chloride and anthropogenic emissions, Geophys. Res. Lett., 39, L10811, doi:10.1029/2012GL051912, 2012.
Pierce, J. R. and Adams, P. J.: Global evaluation of CCN formation by direct emission of sea salt and growth of ultrafine sea-salt, J. Geophys. Res., 111, D06203, doi:10.1029/2005JD006186, 2006.
Piot, M. and von Glasow, R.: The potential importance of frost flowers, recycling on snow, and open leads for ozone depletion events, Atmos. Chem. Phys., 8, 2437–2467, doi:10.5194/acp-8-2437-2008, 2008.
Platt, U., Allan, W., and Lowe, D.: Hemispheric average Cl atom concentration from $^{13}C/^{12}C$ ratios in atmospheric methane, Atmos. Chem. Phys., 4, 2393–2399, doi:10.5194/acp-4-2393-2004, 2004.
Pszenny, A. A. P., Moldanová, J., Keene, W. C., Sander, R., Maben, J. R., Martinez, M., Crutzen, P. J., Perner, D., and Prinn, R. G.: Halogen cycling and aerosol pH in the Hawaiian marine boundary layer, Atmos. Chem. Phys., 4, 147–168, doi:10.5194/acp-4-147-2004, 2004.
Pszenny, A. A. P., Fischer, E. V., Russo, R. S., Sive, B. C., and Varner, R. K.: Estimates of Cl atom concentrations and hydrocarbon kinetic reactivity in surface air at Appledore

ACPD
13, 6067–6129, 2013

Island, Maine (USA), during International Consortium for Atmospheric Research on Transport and Transformation/Chemistry of Halogens at the Isles of Shoals, J. Geophys. Res., 112, D10S13, doi:10.1029/2006JD007725, 2007.

Read, K. A., Majajan, A. S., Carpenter, L. J., Evans, M. J., Faria, B. V. E., Heard, D. E., Hopkins, J. R., Lee, J. D., Moller, S. J., Lewis, A. C., Mendes, L., McQuaid, J. B., Oetjen, H., Saiz-Lopez, A., Pilling, M. J., and Plane, J. M. C.: Extensive halogen mediated ozone destruction over the tropical Atlantic Ocean, Nature, 453, 1232–1235, 2008.

Richter, A., Wittrock, F., Ladstätter-Weißenmayer, A., and Burrows, J. P.: GOME measurements of stratospheric and tropospheric BrO, Adv. Space Res., 29, 1667–1672, 2002.

Riley, J. P., Chester, R., and Duce, R. A.: Chemical oceanography, Vol. 10, in: SEAREX: the Sea/Air Exchange Program, edited by: Riley, J. P. and Chester, R., Academic Press, New York, 1989.

Roscoe, H. K., Brough, N., Jones, A. E., Wittrock, F., Richter, A., Van Roozendael, M., and Hendrick, F.: Resolution of an important discrepancy between remote and in-situ measurements of tropospheric BrO during Antarctic enhancements, Atmos. Meas. Tech. Discuss., 5, 5419–5448, doi:10.5194/amtd-5-5419-2012, 2012.

Rudolph, J., Koppmann, R., and Plass-Duelmer, C.: The budgets of ethane and tetrachloroethene: is there evidence for an impact of reactions with chlorine atoms in the troposphere?, Atmos. Environ., 3010, 1887–1894, 1996.

Ruuskanen, J., Tuch, T., Brink, H., Peters, A., Khlystov, A., Mirme, A., Kos, G. P. A., Brunekreef, B., Wichmann, H. E., Buzorius, G., Vallius, M., Kreyling, W. G., and Pekkanen, J.: Concentrations of ultrafine, fine and $PM_{2.5}$ particles in three European cities, Atmos. Environ., 35, 3729–3738, doi:10.1016/S1352-2310(00)00373-3, 2011.

Saiz-Lopez, A., Plane, J. M. C., and Shillito, J. A.: Bromine oxide in the mid-latitude marine boundary layer, Geophys. Res. Lett., 31, L03111, doi:10.1029/2003GL018956, 2004.

Saiz-Lopez, A., Lamarque, J.-F., Kinnison, D. E., Tilmes, S., Ordóñez, C., Orlando, J. J., Conley, A. J., Plane, J. M. C., Mahajan, A. S., Sousa Santos, G., Atlas, E. L., Blake, D. R., Sander, S. P., Schauffler, S., Thompson, A. M., and Brasseur, G.: Estimating the climate significance of halogen-driven ozone loss in the tropical marine troposphere, Atmos. Chem. Phys., 12, 3939–3949, doi:10.5194/acp-12-3939-2012, 2012.

Salawitch, R. J., Canty, T. P., Kurosu, T. P., Chance, K., Liang, Q., Pawson, S., Bhartia, P. K., Liu, X., Huey, L. G., Dibb, J. E., Simpson, W. R., Donohoue, D., Weinheimer, A. J., Flocke, F. M., Neuman, J., Nowak, J. B., Ryerson, T. B., Oltmans, S. J., Blake, D. R.,

ACPD
13, 6067–6129, 2013

Atlas, E. L., Kinnison, D. E., Tilmes, S., Pan, L., Hendrick, F., van Roozendael, M., Kreher, K., Johnston, P. V., Pierce, R., Crawford, J. H., Jacob, D. J., A da Silva, Nielsen, J. E., Rodriguez, J. M., Liao, J., Stickel, R. E., Tanner, D. J., Knapp, D., Montzka, D., Gao, R. S., Bui, T. P., and Chen, G.: A new interpretation of total column BrO during Arctic spring, Geophys. Res. Lett., 37, L03111, doi:10.1029/2010GL043798, 2010.

Sander, R.: Modeling atmospheric chemistry: interactions between gas-phase species and liquid cloud/aerosol particles, Surv. Geophys., 20, 1–31, 1999.

Sander, R., Rudich, Y., von Glasow, R., and Crutzen, P. J.: The role of $BrNO_3$ in marine tropospheric chemistry: a model study, Geophys. Res. Lett., 26, 2858–2860, 1999.

Sander, R., Keene, W. C., Pszenny, A. A. P., Arimoto, R., Ayers, G. P., Baboukas, E., Cainey, J. M., Crutzen, P. J., Duce, R. A., Hönninger, G., Huebert, B. J., Maenhaut, W., Mihalopoulos, N., Turekian, V. C., and Van Dingenen, R.: Inorganic bromine in the marine boundary layer: a critical review, Atmos. Chem. Phys., 3, 1301–1336, doi:10.5194/acp-3-1301-2003, 2003.

Sander, R., Kerkweg, A., Jöckel, P., and Lelieveld, J.: Technical note: The new comprehensive atmospheric chemistry module MECCA, Atmos. Chem. Phys., 5, 445–450, doi:10.5194/acp-5-445-2005, 2005.

Savoie, D. L., Arimoto, R., Keene, W. C., Prospero, J. M., Duce, R. A., and Galloway, J. N.: Marine biogenic and anthropogenic contributions to non-sea-salt sulfate in the marine boundary layer over the North Atlantic Ocean, J. Geophys. Res., 107, 4356, doi:10.1029/2001JD000970, 2002.

Schwartz, S. E.: Mass-transport considerations pertinent to aqueous phase reactions of gases in liquid-water clouds, in: Chemistry of Multiphase Atmospheric Systems, NATO ASI Series, vol. G6, edited by: Jaeschke, W., Springer Verlag, Berlin, 415–471, 1986.

Simon, H., Kimura, Y., McGaughey, G., Allen, D. T., Brown, S. S., Osthoff, H. D., Roberts, J. M., Byun, R., and Lee, D.: Modeling the impact of $ClNO_2$ on ozone formation in the Houston area, J. Geophys. Res., 114, D00F03, doi:10.1029/2008JD010732, 2009.

Simpson, W. R., von Glasow, R., Riedel, K., Anderson, P., Ariya, P., Bottenheim, J., Burrows, J., Carpenter, L. J., Frieß, U., Goodsite, M. E., Heard, D., Hutterli, M., Jacobi, H.-W., Kaleschke, L., Neff, B., Plane, J., Platt, U., Richter, A., Roscoe, H., Sander, R., Shepson, P., Sodeau, J., Steffen, A., Wagner, T., and Wolff, E.: Halogens and their role in polar boundary-layer ozone depletion, Atmos. Chem. Phys., 7, 4375–4418, doi:10.5194/acp-7-4375-2007, 2007.

ACPD
13, 6067–6129, 2013

Singh, H. B., Gregory, G. L., Anderson, B., Browell, E., Sachse, G. W., Davis, D. D., Crawford, J., Bradshaw, J. D., Talbot, R., Blake, D. R., Thornton, D., Newell, R., Merrill, J.: Low ozone in the marine boundary layer of the tropical Pacific Ocean: photochemical loss, chlorine atoms, and entrainment, J. Geophys. Res., 101, 1907–1917, 1996.

Spracklen, D. V., Pringle, K. J., Carslaw, K. S., Chipperfield, M. P., and Mann, G. W.: A global off-line model of size-resolved aerosol microphysics: I. Model development and prediction of aerosol properties, Atmos. Chem. Phys., 5, 2227–2252, doi:10.5194/acp-5-2227-2005, 2005.

Stanier, C. O., Khlystov, A. Y., and Pandis, S. N.: Ambient aerosol size distributions and number concentrations measured during the Pittsburgh Air Quality Study (PAQS), Atmos. Environ., 38, 3275–3284, 2004.

Tanaka, P. L., Riemer, D. D., Chang, S. H., Yarwood, G., McDonald-Buller, E. C., Apel, E. C., Orlando, J. J., Silva, P. J., Jimenez, J. L., Canagaratna, M. R., Neece, J. D., Mullins, C. B., and Allen, D. T.: Direct evidence for chlorine-enhanced urban ozone formation in Houston, Texas, Atmos. Environ., 37, 1393–1400, 2003.

Textor, C., Schulz, M., Guibert, S., Kinne, S., Balkanski, Y., Bauer, S., Berntsen, T., Berglen, T., Boucher, O., Chin, M., Dentener, F., Diehl, T., Easter, R., Feichter, H., Fillmore, D., Ghan, S., Ginoux, P., Gong, S., Grini, A., Hendricks, J., Horowitz, L., Huang, P., Isaksen, I., Iversen, I., Kloster, S., Koch, D., Kirkevåg, A., Kristjansson, J. E., Krol, M., Lauer, A., Lamarque, J. F., Liu, X., Montanaro, V., Myhre, G., Penner, J., Pitari, G., Reddy, S., Seland, Ø, Stier, P., Takemura, T., and Tie, X.: Analysis and quantification of the diversities of aerosol life cycles within AeroCom, Atmos. Chem. Phys., 6, 1777–1813, doi:10.5194/acp-6-1777-2006, 2006.

Thornton, J. A., Kercher, J. P., Riedel, T. P., Wagner, N. L., Cozic, J., Holloway, J. S., Dubé, W. P., Wolfe, G. M., Quinn, P. K., Middlebrook, A. M., Alexander, B., and Brown, S. S.: A large atomic chlorine source inferred from mid-continental reactive nitrogen chemistry, Nature, 464, 271–274, doi:10.1038/nature08905, 2010.

Toumi, R.: BrO as a sink for dimethylsulfide in the marine atmosphere, Geophys. Res. Lett., 21, 117–120, 1994.

Vignati, E., de Leeuw, G., and Berkowicz, R.: Modeling coastal aerosol transport and effects of surf-produced aerosols on processes in the marine atmospheric boundary layer, J. Geophys. Res., 106, 20225–20238, 2001.

Vogt, R., Crutzen, P. J., and Sander, R.: A mechanism for halogen release from sea-salt aerosol in the remote marine boundary layer, Nature, 383, 327–330, 1996.

ACPD
13, 6067–6129, 2013

von Glasow, R. and Crutzen, P. J.: Model study of multiphase DMS oxidation with a focus on halogens, Atmos. Chem. Phys., 4, 589–608, doi:10.5194/acp-4-589-2004, 2004.
von Glasow R., Sander, R., Bott, A., and Crutzen, P. J.: Modeling halogen chemistry in the marine boundary layer. 2. Interactions with sulfur and cloud-covered MBL, J. Geophys. Res., 107, 4323, doi:10.1029/2001JD000943, 2002.
Wingenter, O. W., Kubo, M. K., Blake, N. J., Smith Jr., T. W., Blake, D. R., and Rowland, F. S.: Hydrocarbon and halocarbon measurements as photochemical and dynamical indicators of atmospheric hydroxyl, atomic chlorine, and vertical mixing obtained during Lagrangian flights, J. Geophys. Res., 101, 4331–4340, 1996.
Wingenter, O. W., Blake, D. R., Blake, N. J., Sive, B. C., Atlas, E., Flocke, F., and Rowland, F. S.: Tropospheric hydroxyl and atomic chlorine concentrations, and mixing time scales determined from hydrocarbon and halocarbon measurements made over the Southern Ocean, J. Geophys. Res., 104, 21819–21828, 1999.
Yang, X., Cox, R. A., Warwick, N. J., Pyle, J. A., Carver, G. D., O'Connor, F. M., and Savage, N. H.: Tropospheric bromine chemistry and its impacts on ozone: a model study, J. Geophys. Res., 110, D23311, doi:10.1029/2005JD006244, 2005.
Zhou, X., Davis, A. J., Kieber, D. J., Keene, W. C., Maben, J. R., Maring, H., Dahl, E. E., Izaguirre, M. A., Sander, R., and Smoydzyn, L.: Photochemical production of hydroxyl radical and hydroperoxides in water extracts of nascent marine aerosols produced by bursting bubbles from Sargasso seawater, Geophys. Res. Lett., 35, L20803, doi:10.1029/2008GL035418, 2008.

ACPD
13, 6067–6129, 2013

Table 1. Global annual mean Na^+ burden, production flux, lifetime, dry and wet deposition fluxes, and global median (and range) aerosol number concentration compared with published results based on other marine aerosol source functions. Uncertainties correspond to year-over-year standard deviation for the 10-yr annual mean.

Study	Na^+ burden (Tg)	Na^+ source (10^3 Tgyr^{-1})	Na^+ lifetime (d)	Na^+ dry dep. (10^3 Tgyr^{-1})	Na^+ wet dep. (10^3 Tgyr^{-1})	Number conc. (cm^{-3})
Hal (this work)	2.5 ± 0.03	1.1 ± 0.02	0.86 ± 0.01	0.49 ± 0.01	0.56 ± 0.01	266 (4.0×10^0–4.4×10^4)
Clarke et al. (2006)	4.0	2.2	0.66	1.5	0.68	
O'dowd et al. (1997)	5.2	4.1	0.47	2.9	1.2	
Mårtensson et al. (2003)	0.55	1.7	1.2	0.061	0.11	
Monahan et al. (1986)	1.2	0.55	0.79	0.34	0.19	
Kerkweg et al. (2008)	2.4	1.7	0.5	0.76	0.90	
Textor et al. (2006)	2.4	1.6	0.5			

ACPD
13, 6067–6129, 2013

Table 2. Median (and range) for total volatile Br (Br_t; pmol mol^{-1}) measured at Hawaii (Pszenny et al., 2004) and along a transect through the eastern North and South Atlantic Oceans (Keene et al., 2009) and statistics simulated for the surface layer within the corresponding grid cells. Reported median and ranges for simulated Br_t along the transect are based on a box bounded by the north–south/east–west limits of the transect segment, as reported in Keene et al. (2009).

Location and time	Measured	Simulated
Hawaii (21° N, 158° W; Sep 1999)	3.7 (< 2–9)	22.7 (19.6–23.4)
NE Atlantic (43–51° N, 2° E–10° W; Oct 2003)	7.2 (3.1–12.3)	17.5 (2.3–63.9)
NE Atlantic (10–33° N,14–20° W; Oct–Nov 2003)	18.8 (8.2–30.1	14.5 (7.2–29.5)
E Atlantic (1–10° N, 13–20° W; Nov 2003)	2.4 (< 0.1–3.1)	12.7 (8.5–22.2)
SE Atlantic (1° N–18° S, 4° E–13° W; Nov 2003)	6.2 (4.4–10.1)	17.5 (0.1–44.4)

ACPD
13, 6067–6129, 2013

Table 3. Measured and simulated BrO mixing ratios (pmol mol^{-1}) ± standard deviations (when available) for sites reported by Sander et al. (2003; Table 4) and Read et al. (2008). Simulated results are based on 10-yr temporal means for the surface layer during the sampling month and within the grid-box corresponding to the measurements.

Location and time	Measured	Simulated	Day/night	Est. daytime mean
Hawaii (20° N, 155° W; Sep 1999)	< 2	2.2 ± 0.20	1.96	4.2 ± 0.39
Finokalia, Crete (35° N, 26° E; Jul–Aug 2000)	< 0.7–1.5	0.072 ± 0.040	1.68	0.12 ± 0.067
Made Head, Ireland (53° N, 10° W; Apr–May 1997)	1.1–2.5	1.1 ± 0.41	1.60	1.7 ± 0.66
Made Head, Ireland (53° N, 10° W; Sep–Oct 1998)	< 1	0.96 ± 0.49	2.04	2.0 ± 1.0
Tenerife, Canary Islands (29° N, 17° W; Jun–Jul 1997)	3	3.0 ± 0.53	1.71	5.2 ± 0.9
Weybourne, Great Britain (53° N, 1° E; Oct 1996)	< 2	0.018 ± 0.006	2.29	0.040 ± 0.013
São Vicente, Cape Verde (17° N, 25° W; Oct 2006–Oct 2007)	2.5 ± 1.1*	2.9 ± 0.93	2.00	5.7 ± 2.4

* Maximum daytime values reported by Read et al. (2008). Nighttime values were below detection limits (0.5–1.0 pmol mol^{-1}).

ACPD
13, 6067–6129, 2013

Table 4. Percentage contribution of different production pathways for atomic Br versus sum of all pathways based on ANN climatological means for different regions of the atmosphere.

	PBL	FT	Trop.	NH CBL	SH CBL	NH MBL	SH MBL
$BrO + NO \rightarrow Br + NO_2$	22 %	30 %	26 %	61 %	54 %	27 %	12 %
$HOBr + h\nu \rightarrow Br + OH$	12 %	27 %	19 %	5.6 %	7 %	9 %	12 %
$BrCl + h\nu \rightarrow Br + Cl$	18 %	8.5 %	14 %	9.9 %	9.2 %	23 %	15 %
$Br_2 + h\nu \rightarrow Br + Br$	18 %	11 %	15 %	18 %	21 %	17 %	21 %
$BrO + BrO \rightarrow 2Br + O_2$	15 %	11 %	13 %	3.0 %	5.9 %	8.4 %	23 %
$BrO + ClO \rightarrow Br + OClO$	5.0 %	5.8 %	5.3 %	1.0 %	0.4 %	5.4 %	3.3 %
$BrO + ClO \rightarrow Br + Cl + O_2$	4.3 %	4.9 %	4.4 %	0.8 %	0.4 %	4.8 %	2.9 %
$BrO + DMS \rightarrow DMSO + Br$	2.9 %	0.3 %	1.8 %	0.1 %	0.5 %	3.2 %	8.0 %
$BrO + CH_3O_2 \rightarrow Br + HCHO + HO_2$	2.0 %	1.0 %	1.6 %	0.4 %	0.4 %	2.1 %	2.1 %
$BrNO_2 + h\nu \rightarrow Br + NO_2$	0.0 %	0.0 %	0.0 %	0.4 %	0.3 %	0.0 %	0.0 %

ACPD
13, 6067–6129, 2013

Table 5. Relative contributions of different pathways to total direct O_3 destruction in *Hal* and in *NoHal* simulations and the corresponding total O_3 destruction via all pathways in *Hal* relative to *NoHal* simulations expressed as percentages; based on ANN means for different regions of the atmosphere.

	PBL	FT	NH CBL	SH CBL	NH MBL	SH MBL
Hal						
$R_{O_3+h\nu}/R_{\text{Hal Total}}$	60 %	41 %	30 %	34 %	66 %	74 %
$R_{O_3+NO}/R_{\text{Hal Total}}$	32 %	39 %	68 %	60 %	28 %	8.1 %
$R_{O_3+Br}/R_{\text{Hal Total}}$	6.2 %	15 %	0.8 %	1.3 %	4.4 %	16 %
$R_{O_3+Cl}/R_{\text{Hal Total}}$	0.6 %	0.9 %	0.2 %	0.1 %	0.7 %	0.7 %
NoHal						
$R_{O_3+h\nu}/R_{\text{NoHal Total}}$	76 %	56 %	71 %	38 %	47 %	78 %
$R_{O_3+NO}/R_{\text{NoHal Total}}$	23 %	40 %	27 %	60 %	49 %	21 %
$R_{\text{Hal Total}}/R_{\text{NoHal Total}}$ *	58 %	76 %	81 %	74 %	57 %	38 %

* Relatively lower rates of direct O_3 destruction via all pathways in *Hal* simulations are driven in part by relatively lower steady-state O_3 mixing ratios (see Fig. 7).

ACPD
13, 6067–6129, 2013

Table 6. WOUDC stations (and corresponding periods of record) at which the vertical profiles in O_3 evaluated herein were measured.

Station code	Station name	LAT	LON	Altitude (m)	Start date	Stop date
21	Edmonton	53.6	−114	766	Jan 1980	Dec 1993
24	Resolute	74.7	−95.0	40	Jan 1980	Dec 1993
67	Boulder	40.0	−105	1634	Jan 1985	Dec 1993
432	Tahiti	−18.0	−149	2	Jan 1998	Dec 1999
175	Nairobi	−1.27	36.9	1795	Jan 1998	Dec 2001
434	San Cristobal	−0.92	−89.6	8	Mar 1998	Dec 2001
435	Paramaribo	5.81	−55.2	25	Oct 1999	Dec 2001
191	Samoa	−14.3	−170	82	Apr 1986	Dec 2002
219	Natal	−5.84	−35.2	32	Jan 1998	Dec 2002
265	Pretoria	−25.6	28.2	1524	Jul 1990	Dec 2002
436	Reunion	−21.1	55.5	24	Jan 1998	Dec 2002
448	Malindi	−2.99	40.2	−6	Mar 1999	Dec 2002
437	Java	−7.57	112	50	Jan 1998	Nov 2002
438	Fiji	−18.1	178	6	Jan 1998	Nov 2002

ACPD
13, 6067–6129, 2013

Table 7. Global annual budgets for SO_2, H_2SO_4, nss-SO_4^{2-}, and DMS, for *Hal*, *NoHal* simulations, and a 5-yr simulation using 3-mode modal-CAM (v3.6.33) with its standard chemical module. Ranges of results from previous studies are shown for comparison.

		Hal	*NoHal*	CAM 3.6.33	Previous studies
		SO_2			
Sources ($TgSy^{-1}$)		79.3	80.6	84.4	83.0–124.6[b]
	Emission	67.5	67.5	67.5	63.7–92.0[a]
	DMS oxidation	11.8	13.1	16.9	10.0–24.7[a]
Sink ($TgSy^{-1}$)		80.5	82.8	87.0	
	Dry deposition	20.3	21.4	22.5	16.0–55.0[a]
	Wet deposition	14.7	13.8	14.6	0.0–19.9[a]
	Gas oxidation	6.2	6.4	11.9	6.1–16.8[a]
	Aqueous oxidation	39.3	41.2	38.0	24.5–57.8[a]
Burden (TgS)		0.57	0.57	0.31	0.20–0.61[a]
Lifetime (d)		2.6	2.6	1.5	0.60–2.6[a]
		H_2SO_4			
Source:	SO_2 + OH	6.2	6.4	11.9	6.1–22.0[a]
Sink ($TgSy^{-1}$)		5.9	6.2	11.8	
	Nucleation	1.2	1.3	0.01	0.05–0.07[b]
	Condensation	4.6	4.8	10.9	13.0–15.2[b]
	Cloud scavenging	0.1	0.1	0.9	
Burden (TgS)		0.0029	0.0032	1.2×10^{-3}	9.0×10^{6}–0.001[a]
Lifetime (h)		4.1	4.4	0.086	0.12–0.17[a]
		nss-SO_4^{2-}			
Sources ($TgSy^{-1}$)		46.9	49.1	50.6	59.7 ± 13.2[a]
	Emission	1.7	1.7	1.7	
	Aqueous S(IV) oxidation	39.3	41.2	38.0	
	Microphysics[c]	5.9	6.2	10.9	
Sink ($TgSy^{-1}$)		45.1	47.3	51.8	
	Dry Deposition	11.8	12.7	10.3	
	Wet Deposition	33.3	34.6	41.5	
Burden (TgS)		0.86	0.88	0.67	0.66 ± 0.17[a]
Lifetime (h)		5.6	5.4	4.8	4.1 ± 0.74[a]
		DMS			
Sources:	Emission ($TgSy^{-1}$)	18.3	18.3	18.3	10.7–23.7[a]
Sinks:	Gas oxidation ($TgSy^{-1}$)	18.3	18.3	18.4	
Burden (TgS)		0.032	0.15	0.029	0.02–0.15[a]
Lifetime (h)		0.64	3.0	0.57	0.024–0.13[a]

[a] From Liu et al. (2012) and references therein.
[b] From Spracklen et al. (2005) and references therein.
[c] Combined source of nss-SO_4^{2-} due to $H_2SO_{4(g)}$ nucleation, condensation, and scavenging.

ACPD
13, 6067–6129, 2013

Table 8. Relative contributions of different reaction pathways (R) to total DMS and S(IV) oxidation in *Hal* and in *NoHal* simulations and the corresponding total DMS and S(IV) oxidation via all pathways in *Hal* versus *NoHal* simulations expressed as percentages; based on ANN means, and spatial medians for different regions of the atmosphere. Subscripts aq and cl designate aerosol and cloud-water reactions, respectively.

	PBL	FT	Troposphere	NH CBL	SH CBL	NH MBL	SH MBL
DMS(*Hal*)							
$R_{DMS + OH}/R_{DMS\text{-}Hal\text{-}Total}$	6.6 %	27 %	8.3 %	9.3 %	18 %	12 %	4.0 %
$R_{DMS+NO_3}/R_{DMS\text{-}Hal\text{-}Total}$	11 %	14 %	11 %	69 %	53 %	24 %	3.8 %
$R_{DMS + Cl}/R_{DMS\text{-}Hal\text{-}Total}$	14 %	8.4 %	14 %	9.3 %	5.0 %	20 %	9.1 %
$R_{DMS + BrO}/R_{DMS\text{-}Hal\text{-}Total}$	68 %	50 %	67 %	12 %	24 %	44 %	82 %
DMS(*NoHal*)							
$R_{DMS + OH}/R_{DMS\text{-}NoHal\text{-}Total}$	54 %	74 %	57 %	13 %	31 %	34 %	66 %
$R_{DMS+NO_3}/R_{DMS\text{-}NoHal\text{-}Total}$	46 %	26 %	43 %	87 %	69 %	66 %	34 %
$R_{DMS\text{-}Hal\text{-}Total}/R_{DMS\text{-}NoHal\text{-}Total}^{*}$	140 %	52 %	122 %	73 %	43 %	118 %	227 %
S(IV)(*Hal*)							
$R_{SO_2+OH}/R_{S(IV)Total}$	11 %	13 %	11 %	11 %	5.7 %	18 %	6.5 %
$R_{S(IV)aq+H_2O_2}/R_{S(IV)\text{-}Hal\text{-}Total}$	1.3 %	0.6 %	1.2 %	1.0 %	0.2 %	2.3 %	2.0 %
$R_{S(IV)aq+O_3}/R_{S(IV)\text{-}Hal\text{-}Total}$	0.1 %	0.0 %	0.1 %	0.0 %	0.1 %	0.0 %	0.8 %
$R_{S(IV)aq+HOCl}/R_{S(IV)\text{-}Hal\text{-}Total}$	0.9 %	0.2 %	0.8 %	0.1 %	0.0 %	2.0 %	4.9 %
$R_{S(IV)aq + HOBr}/R_{S(IV)\text{-}Hal\text{-}Total}$	0.2 %	0.1 %	0.2 %	0.0 %	0.0 %	0.0 %	2.0 %
$R_{S(IV)cl+H_2O_2}/R_{S(IV)\text{-}Hal\text{-}Total}$	74 %	81 %	75 %	60 %	90 %	73 %	81 %
$R_{S(IV)cl+O_3}/R_{S(IV)\text{-}Hal\text{-}Total}$	12 %	1.9 %	11 %	27 %	4.2 %	4.8 %	2.1 %
$R_{S(IV)cl + HOCl}/R_{S(IV)\text{-}Hal\text{-}Total}$	0.2 %	1.3 %	0.4 %	0.1 %	0.0 %	0.0 %	0.2 %
$R_{S(IV)cl + HOBr}/R_{S(IV)\text{-}Hal\text{-}Total}$	0.6 %	1.8 %	0.8 %	0.8 %	0.2 %	0.2 %	0.5 %
$R_{S(IV)aq}/R_{S(IV)cl}$	2.8 %	1.1 %	2.6 %	1.4 %	0.3 %	5.6 %	12 %
S(IV)(*NoHal*)							
$R_{SO_2+OH}/R_{S(IV)\text{-}NoHal\text{-}Total}$	10 %	14 %	11 %	8.5 %	5.0 %	17 %	9.1 %
$R_{S(IV)aq+H_2O_2}/R_{S(IV)\text{-}NoHal\text{-}Total}$	1.1 %	0.5 %	1.0 %	0.8 %	0.1 %	1.5 %	1.9 %
$R_{S(IV)aq+O_3}/R_{S(IV)\text{-}NoHal\text{-}Total}$	0.2 %	0.0 %	0.2 %	0.0 %	0.0 %	0.0 %	3.1 %
$R_{S(IV)cl+H_2O_2}/R_{S(IV)\text{-}NoHal\text{-}Total}$	76 %	81 %	76 %	59 %	90 %	74 %	83 %
$R_{S(IV)cl+O_3}/R_{S(IV)\text{-}NoHal\text{-}Total}$	13 %	5.1 %	12 %	31 %	5.3 %	7.5 %	2.8 %
$R_{S(IV)aq}/R_{S(IV)cl}$	1.5 %	0.6 %	1.4 %	0.9 %	0.1 %	1.9 %	5.9 %
$R_{S(IV)\text{-}Hal\text{-}Total}/R_{S(IV)\text{-}NoHal\text{-}Total}^{*}$	88 %	88 %	89 %	88 %	87 %	86 %	89 %

[*] Differences are driven in part by corresponding differences in steady state concentrations of DMS and S(IV) in *Hal* and *NoHal* simulation.

ACPD
13, 6067–6129, 2013

Table 9. Mean particle number concentrations ± standard deviations when available (cm^{-3}) measured at surface locations and the median, range, mean and log_{10}-normal standard deviation for number concentrations simulated with *Hal* in the surface layer of the corresponding grid cells. Simulated values are summed across all three particle modes.

	Simulated (*Hal*)					
Location	Observed	Median	Max	Min	Mean ($\pm 10^{\sigma}$)	Source
Alkmaar, Netherlands	25 800 ± 11 300	2597	23 508	815	$2814 \pm 10^{9.4\%}$	Ruuskanen et al. (2001)
Erfurt, Germany	25 900 ± 12 200	2767	35 180	759	$2977 \pm 10^{11.8\%}$	Ruuskanen et al. (2001)
Helsinki, Finland	20 300 ± 8200	26 28	13 134	610	$2839 \pm 10^{11.0\%}$	Ruuskanen et al. (2001)
Pittsburg, PA, USA	16 470	13 037	48 678	2592	$12\,566 \pm 10^{8.0\%}$	Stanier et al. (2004)
Beijing, PRC	29 000 ± 10 000	11 340	66 393	1697	$11\,082 \pm 10^{7.5\%}$	Leitte et al. (2011)
Indian Ocean (North of ITCZ)	856 ± 232	324	1393	151	$387 \pm 10^{7.9\%}$	Kamra et al. (2003)
Indian Ocean (ITCZ)	418 ± 151	232	1277	74	$248 \pm 10^{7.1\%}$	Kamra et al. (2003)
Indian Ocean (South of ITCZ)	334 ± 20	277	884	104	$309 \pm 10^{6.8\%}$	Kamra et al. (2003)
Melpitz, Germany	4830	2767	35 180	759	$2977 \pm 10^{11.8\%}$	Birmili et al. (2001)*
Hyytiälä, Finland	1813 ± 1525	1708	7846	415	$1693 \pm 10^{10.7\%}$	Mäkelä et al. (2000)

* As reported by Spracklen et al. (2005).

ACPD
13, 6067–6129, 2013

Table 10. Correlation coefficients (R), normalized mean square error (NMSE), and mean deviations of measured SO_2(g) and nss-SO_4^{2-} versus mean simulated values in the surface layer of the corresponding grid cell with *Hal* and *NoHal*, as plotted in Fig. 13. Continental measurements are from the IMPROVE network; and marine measurements are from the Atmosphere-Ocean Chemistry Experiment (AEROCE, Savoie et al., 2002), US Department of Energy as the Environmental Measurements Laboratory (DOE-EML), and the Sea-Air Exchange Experiment (SEAREX, Riley et al., 1989).

		R	NMSE	Mean deviation
Hal	SO_2(g)	0.53	2.9	2.7 (±8.8)
	Continental nss-SO_4^{2-}	0.87	0.083	0.59 (±2.0)
	Marine nss-SO_4^{2-}	0.93	0.083	1.9 (±2.6)
NoHal	$SO_{2(g)}$	0.54	2.8	2.6 (±8.8)
	Continental nss-SO_4^{2-}	0.82	0.095	0.55 (±2.2)
	Marine nss-SO_4^{2-}	0.89	0.086	2.1 (±2.6)

ACPD
13, 6067–6129, 2013

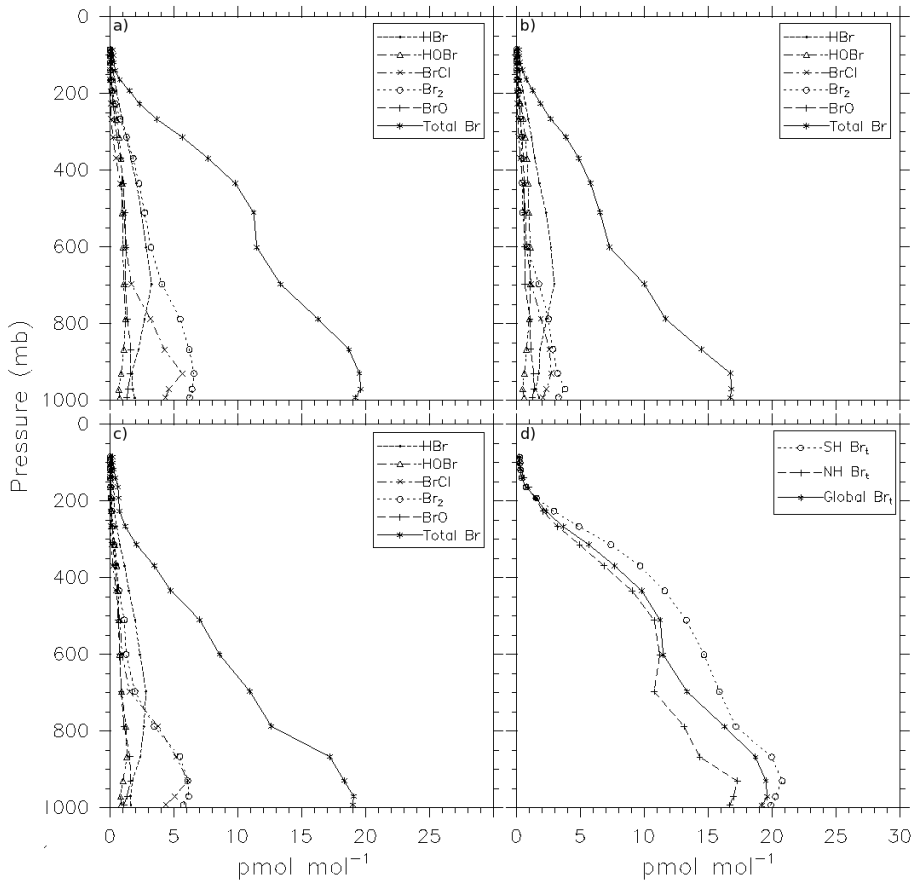

Fig. 1. Spatial median vertical profiles of Br_t and its component gases for **(a)** ANN, **(b)** JJA, and **(c)** DJF; **(d)** ANN Br_t for NH, SH and global regions.

ACPD
13, 6067–6129, 2013

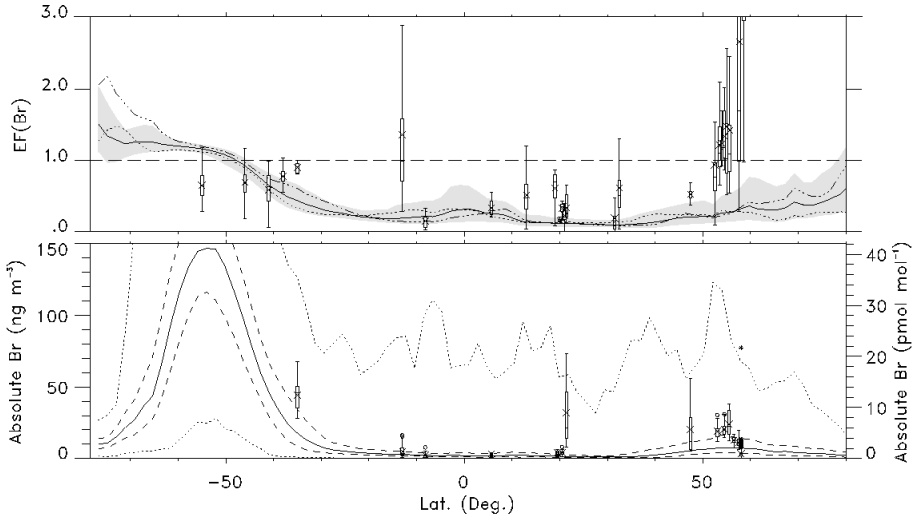

Fig. 2. Simulated zonal (a) EF(Br) and (b) absolute Br^- concentration and the corresponding measurement values reported by Sander et al. (2003) and Keene et al. (2009). See Appendix A for a listing of measurement sources. Box-and-whiskers indicate minimum, 25th quartile, median, 75th quartile and maximum values where maxima and minima are of data within 1.5 times the 25th–75th quartile range. Crosses indicate means. In (a), simulated media are indicated by the solid line, the shaded area depicts 25th–75th quartile range, the dash-dotted line depicts the JJA median, and the dotted line depicts the DJF median. The horizontal dashed line indicates unity (i.e. no enrichment or depletion relative to conservative sea-salt species). In (b) simulated media are indicated by the solid line, 25th and 75th quartiles by the dashed lines, and maxima and minima by the dotted lines.

ACPD
13, 6067–6129, 2013

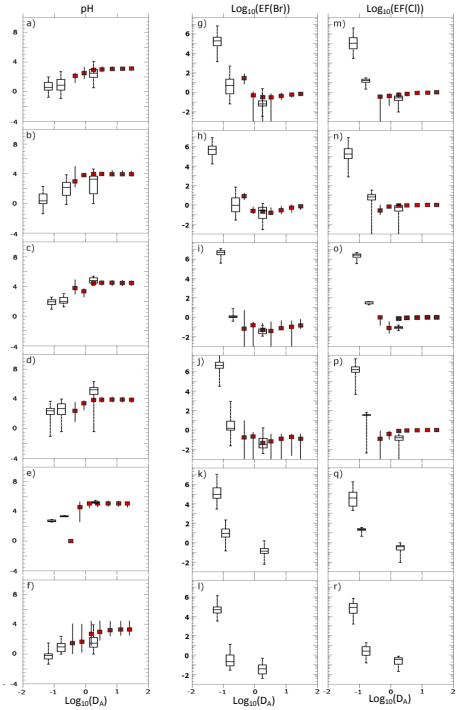

Fig. 3. Size-resolved **(a–f)** pH inferred from measurements; and **(g–l)** (where available) measured EF(Br); and **(m–r)** EF(Cl), in black line with red fill, and the corresponding values simulated with *Hal* in black line with open fill. Box-and-whiskers depict maximum, 75th quartile, median, 25th quartile, and minimum values. D_A is the ambient particle diameter in μm. The top four rows correspond to the regions in the eastern North and South Atlantic Oceans reported by Keene et al. (2009): row 1 is EURO, 2 is NAFR, 3 is ITCZ, and 4 is SATL. Row 5 corresponds to Hawaii (Pszenny et al., 2004), and row 6 corresponds to the New England Air Quality Study (NEAQS) along the US East Coast (Keene et al., 2004).

ACPD
13, 6067–6129, 2013

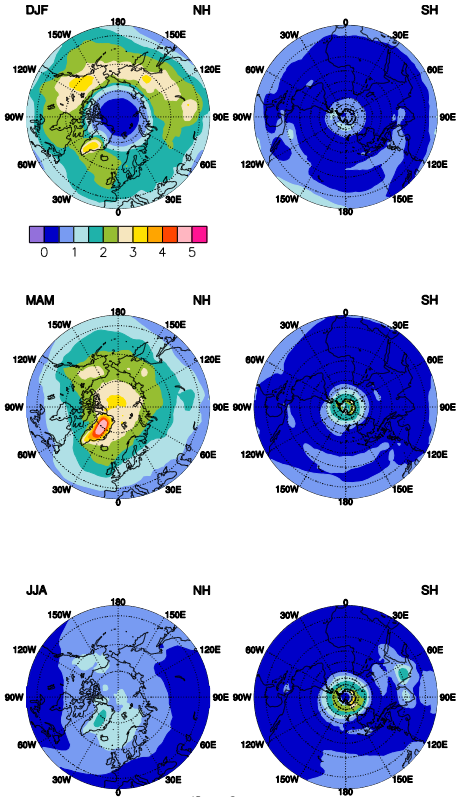

Fig. 4. Vertically integrated BrO (10^{13} cm^{-2}) for the Northern and Southern Hemispheres (NH, SH), averaged over winter (DJF), spring (MAM; March-April-May), and summer (JJA).

ACPD
13, 6067–6129, 2013

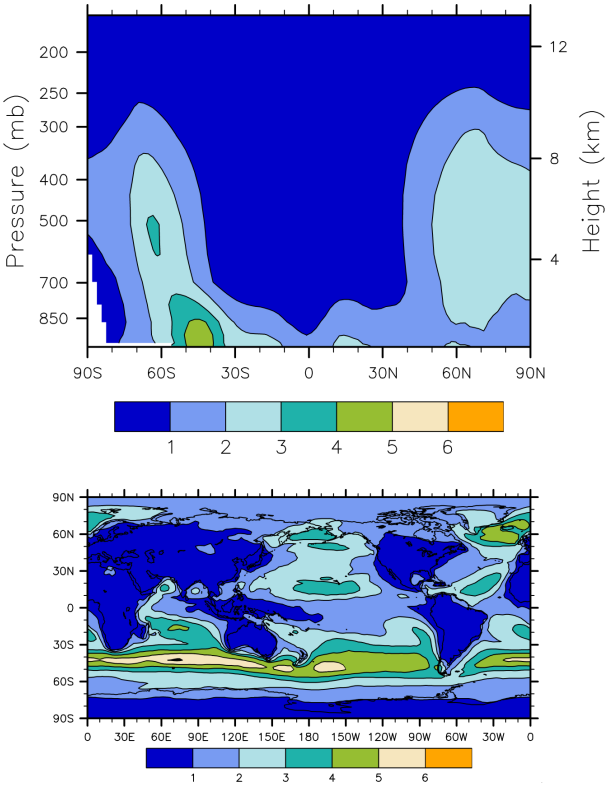

Fig. 5. Annual mean (a) zonal and (b) PBL BrO mixing ratios (pmol mol^{-1}).

ACPD
13, 6067–6129, 2013

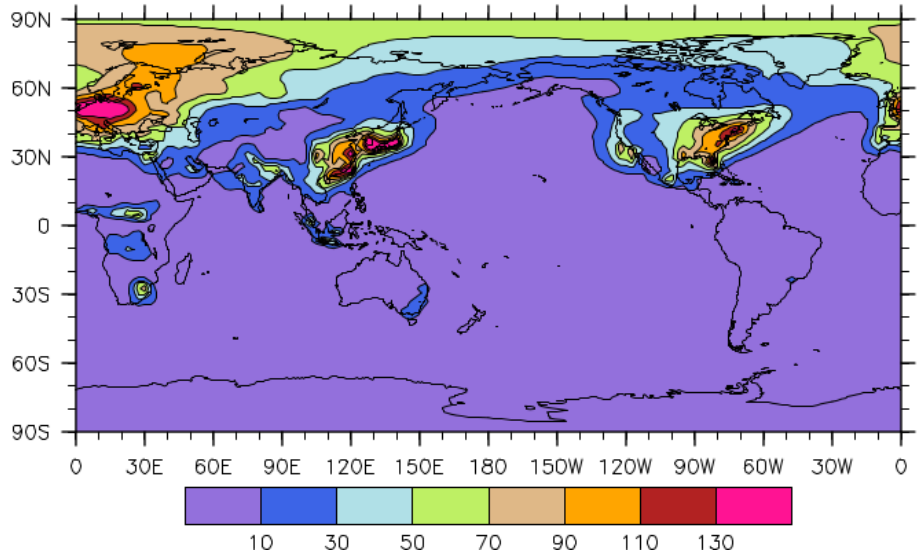

Fig. 6. ANN-PBL $ClNO_2$ mixing ratio (pmol mol^{-1}).

ACPD
13, 6067–6129, 2013

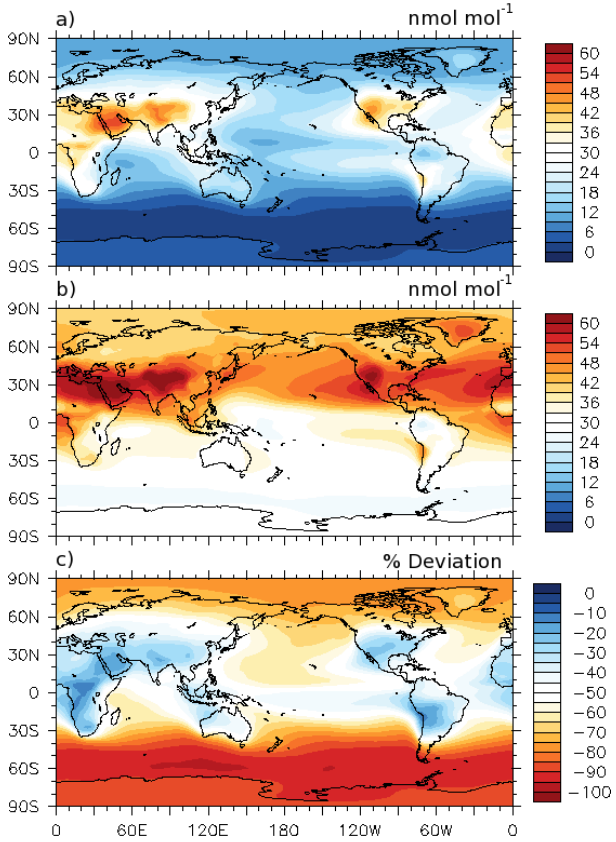

Fig. 7. ANN-PBL O_3 (nmol mol^{-1}) for **(a)** *Hal* and **(b)** *NoHal*, and **(c)** the corresponding percent deviations.

ACPD
13, 6067–6129, 2013

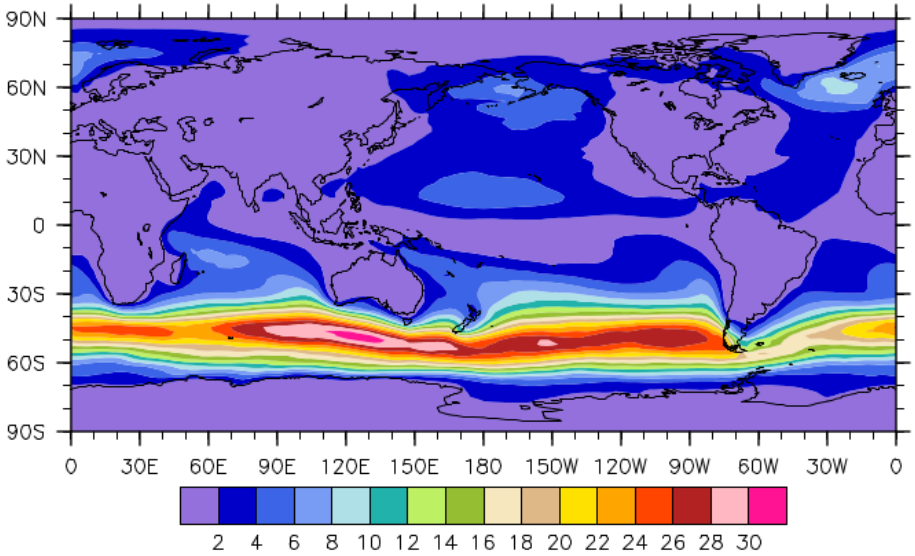

Fig. 8. Percent contribution of $Br + O_3$ to total O_3 destruction in PBL (see Table 5).

ACPD
13, 6067–6129, 2013

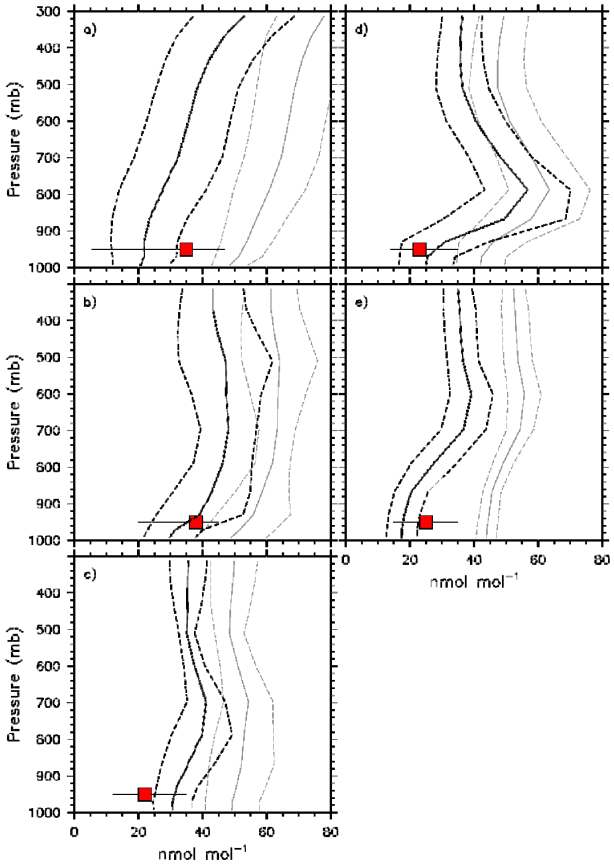

Fig. 9. Vertical profiles of mean O_3 (nmol mol^{-1}; solid) and standard deviation (dashed) simulated with *Hal* (black) and *NoHal* (gray) and the corresponding mean O_3 measured in near-surface air (red boxes) for the **(a)** EURO, **(b)** NAFR, **(c)** ITCZ, and **(d)** SATL regimes as reported by Keene et al. (2009) and at **(e)** Hawaii (Pszenny et al., 2004). Bars depict measurement ranges.

ACPD
13, 6067–6129, 2013

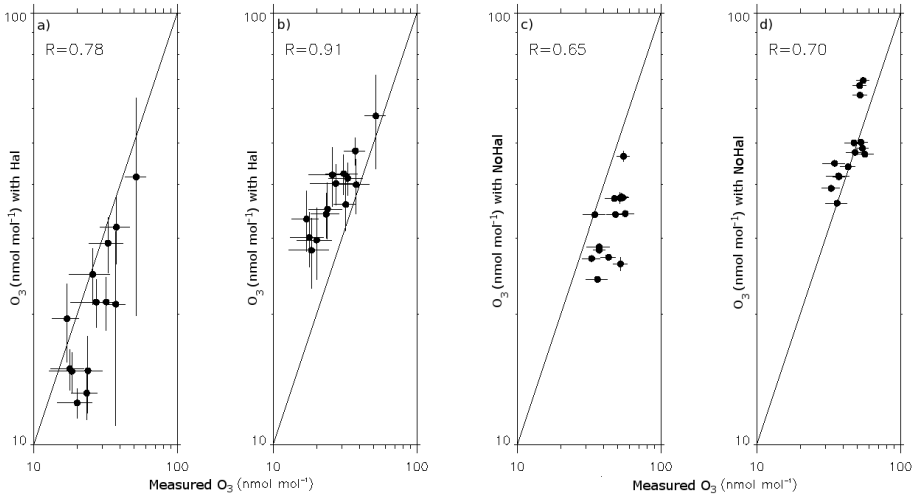

Fig. 10. O_3 simulated in the PBL with **(a)** *Hal*, and **(b)** *NoHal* and at the 500 mb pressure height for **(c)** *Hal* and **(d)** *NoHal* versus the WOUDC O_3 climatology. Horizontal and vertical bars represent measurement and simulated standard deviations, respectively. The corresponding correlation coefficients (R) are shown.

ACPD
13, 6067–6129, 2013

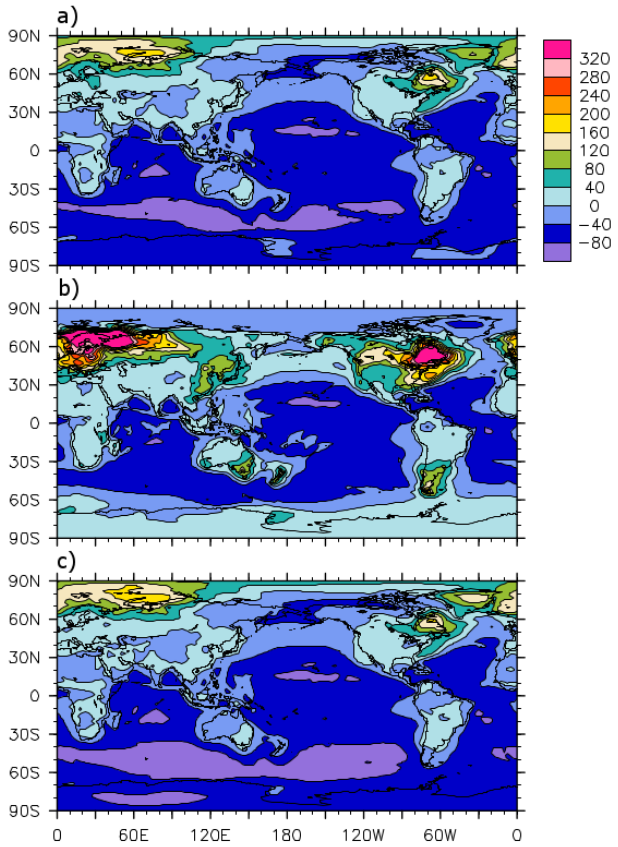

Fig. 11. Percent deviation of **(a)** NO_x ($NO + NO_2$), **(b)** NO, and **(c)** NO_2 in the PBL for *Hal* versus *NoHal* simulations.

ACPD
13, 6067–6129, 2013

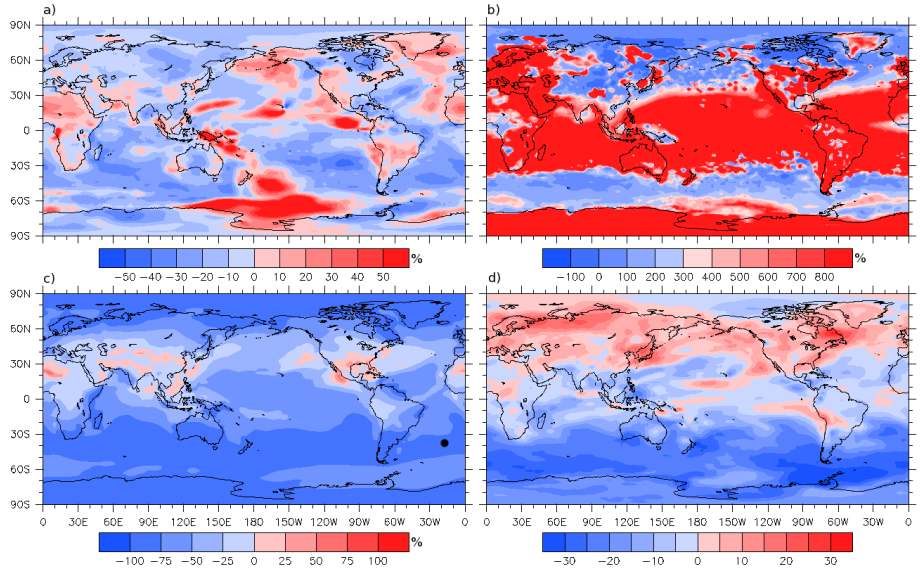

Fig. 12. Percent deviations in ANN-PBL **(a)** SO_2, **(b)** aggregate aqueous S(IV) ($SO_{2(aq)}$, HSO_3^-, and SO_3^{2-} summed over the three simulated size bins), **(c)** DMS and **(d)** aggregate nss-SO_4.

ACPD
13, 6067–6129, 2013

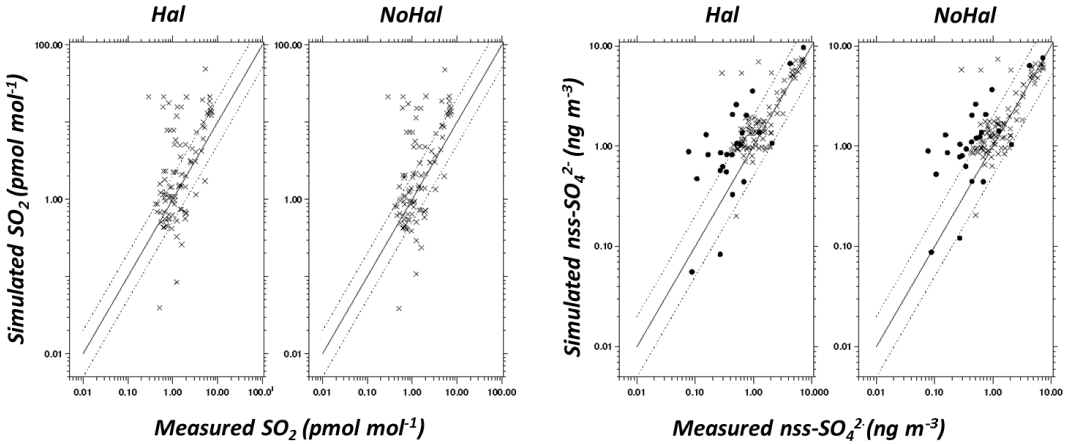

Fig. 13. Mean SO_2 measured by the IMPROVE network at continental sites in the US versus mean SO_2 in the surface layer of the corresponding grid cell simulated with (a) *Hal* and (b) *NoHal*. Mean nss-SO_4^{2-} measured at continental sites by the IMPROVE network (designated by x's) and at marine sites by Atmosphere-Ocean Chemistry Experiment (AEROCE, Savoie et al., 2002), US Department of Energy as the Environmental Measurements Laboratory (DOE-EML), and the Sea-Air Exchange Experiment (SEAREX, Riley et al., 1989) (designated by dark circles) versus mean nss-SO_4^{2-} in the surface layer of the corresponding grid cells simulated with (c) *Hal* and (d) *NoHal*.

ACPD
13, 6067–6129, 2013